# COMBUSTION SYNTHESIS AND THERMOELECTRIC PROPERTIES OF BETA-GALLIA RUTILE INTERGROWTHS

BY

MICHAEL ALBERGA

A THESIS
SUBMITTED TO THE FACULTY OF

ALFRED UNIVERSITY

IN PARTIAL FULFILLMENT OF THE REQUIREMENTS
FOR THE DEGREE OF

MASTER OF SCIENCE

IN

MATERIALS SCIENCE AND ENGINEERING

ALFRED, NEW YORK

JUNE, 2016

COMBUSTION SYNTHESIS AND THERMOELECTRIC PROPERTIES OF BETA-GALLIA RUTILE INTERGROWTHS

BY

MICHAEL ALBERGA

ALFRED UNIVERSITY 2016

SIGNATURE OF AUTHOR_____

APPROVED BY_____

DOREEN D. EDWARDS, ADVISOR

_____

SCOTT T. MISTURE, ADVISORY COMMITTEE

_____

DAVID W. LIPKE, ADVISORY COMMITTEE

_____

CHAIR, ORAL THESIS DEFENSE

ACCEPTED BY_____

DOREEN D. EDWARDS, DEAN
KAZUO INAMORI SCHOOL OF ENGINEERING

# ACKNOWLEDGMENTS

First, I want to thank my Advisor, Dr. Doreen Edwards. Throughout my time in graduate school she has been my guide; insightful, supportive, and encouraging. Whether looking for guidance on my thesis work, advice about careers, or to just chat about life, her door has always been open. Thank you so much, Doreen!

I would also like to thank Dr. Misture and Dr. Lipke for their guidance through my thesis research, as well as Fran Williams and Gerry Wynick for their work with the equipment over the years.

Thank you Mom and Dad for all of your support over the many, many years I've spent in school. Aunt Kathy, you've been there whenever I've needed you. You've helped guide me though some rough times, and I'm so thankful to have you in my life.

Braeden and Higgs, you two have been the best friends that I could have ever asked for! Seriously, I consider myself fortunate to have become so close with both of you. You've made my time in Alfred a blast!

Higgs, Claire, and Ana, Team Edwards will ALWAYS live on! And the same goes for the Claire and Mike Show!

Katie, you've helped me with so many things over the years that I've lost count! You're the best! Thank you so much!

Finally, I'd like to thank Dr. Schulze, Dr. Pilgrim, Tiffany Horton, Kevin, Peter, Pete, Trevyn, and Kyle.

Table of Contents

# LIST OF TABLES

**Page**

# LIST OF FIGURES

**Page**

# ABSTRACT

Beta-gallia rutile intergrowth materials (BGRs), a homologous series following $Ga_4Ti_{n-4}O_{2n-2}$ ($15 \leq n \leq 25$, odd), were investigated as potential n-type thermoelectric device candidates given their structural similarities to the strontium titanate Ruddlesden-Popper phases and misfit layer cobaltite materials. Compositions from n=15 through 25 (odd) were synthesized using solution combustion synthesis (C.S.). For comparison a sample of n=19 was prepared with solid-state synthesis (S.S.). The combustion synthesis yielded nanopowder samples of the anatase phase, which were transformed into the intergrowth phase after heating at 1400 °C in air. The X-ray diffraction analysis of the heat treated powder samples showed that the n=23 and 25 samples had rutile impurities and the n=15 had β-$Ga_2O_3$ impurities. Spark plasma sintering (SPS) produced reduced samples with highly dense microstructures, free of impurity rutile. β-$Ga_2O_3$, however, was still present in the n=15 sample. A systematic shifting the position of the diffraction peaks to higher angles was noted between the pre- and post-sintered samples, indicating a decrease in the unit cell size.

Below 400 °C thermopower measured in argon was not temperature dependent, indicating the lack of thermally generated charge carriers. Combined with the increase in electrical conductivity with temperature, it was concluded that these BGR materials are polaron conductors, with mobility activation energies of 0.052 eV. Above 400 °C BGR begins to break down in to rutile and β-$Ga_2O_3$. Overall there is no discernable trend between electrical conductivity and composition, although in general thermopower increases with increasing n-value from 15 to 23. No conclusions could be drawn regarding thermal conductivity and composition due to the scatter in the thermal diffusivity data.

The electrical conductivity of the C.S. samples were an order of magnitude lower than the S.S. sample, and the thermopower was higher. The lower carrier concentration in C.S. samples is hypothesized to be caused by nitrogen impurities – a byproduct of combustion synthesis –acting as acceptor-type substitutional dopants in the oxygen sublattice. Among the samples investigated, the n=19 S.S. sample showed the highest power factor ($\alpha^2\sigma$) and a higher ZT of 0.02 at 400 °C.

# I. INTRODUCTION

## A. Thermoelectric Materials and Devices

In 1822 Thomas Johann Seebeck discovered that when two dissimilar materials are joined together in a closed circuit and the junction between them heated, a small electric current is generated[1-3]. Further, he noticed that when two junctions were heated with a temperature difference between them, the resulting voltage which developed was proportional to the difference in temperature[2,3]. This became known as the Seebeck effect, and is the basis of the thermoelectric effect and the operation of thermocouples.

Similar to the Seebeck effect is the Peltier effect, which states that a heat source or sink can be created if a current is passed through the junction. Whether a junction behaves as a heat source or a heat sink is simply dependent on the direction in which the current is passed through said junction. The Thompson effect, another effect related to the Seebeck effect, states that a voltage develops along a material when it is placed in a temperature gradient[1].

Thermoelectric generators (TEGs) were thus developed and harness the Seebeck effect, with the goal of recovering electricity from heat which would otherwise be wasted. TEGs involve two main semiconductor components, one n-type and the other p-type, arranged to be electrically in series and thermally in parallel, seen in Figure 1. As seen in the schematic drawing, charge carriers in both semiconductor components migrate to the hot side of the module due to the higher energy state at that end. The potential generated across a couple can then be used to drive a current through an electronic device. The most notable historic uses of these devices are as radioisotope thermoelectric generators, or RTGs. These devices were usually composed of bismuth telluride, silicon germanium, or TAGS (tellurium, silver, germanium, and antimony) thermoelectric alloys. Notable uses of RTGs include the Cassini, Ulysses, Galileo, and Voyager space probes, the Viking Mars lander, Pioneer 10 and 11, and the Apollo lunar missions. Over decades these devices have proven to be reliable sources of power, radiation-resistant, scalable, and

rugged[2,4]. Additionally, the solid-state nature of RTGs is advantageous in that there are no moving (mechanical) parts, thereby reducing the likelihood of breakdown[5].

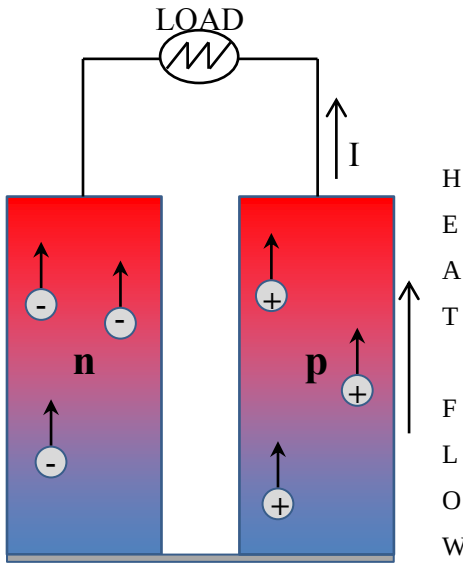


Figure 1. Schematic drawing of a single thermoelectric generator couple.

When comparing the performance of different thermoelectric materials at different temperatures, a dimensionless figure of merit called ZT is used, seen below.

$$ZT = \frac{\alpha^2 \sigma}{\kappa} T = \frac{\alpha^2}{\rho \cdot \kappa} T \quad (1)$$

In this equation, α is the Seebeck coefficient (V/K), σ is the electrical conductivity ($\Omega^{-1}m^{-1}$), ρ is electrical resistivity (1/σ, Ω·m), and κ is the thermal conductivity (W/m·K), which can be represented by $\kappa = \kappa_E + \kappa_L$ where $\kappa_E$ and $\kappa_L$ are the electronic and lattice contributions to thermal conductivity, respectively[2,3,5]. A higher ZT indicates better thermoelectric performance, and is generally achieved by either maximizing what is referred to as the power factor ($\alpha^2\sigma$) or minimizing the thermal conductivity.

Since ZT in equation 1 is representative of only the thermoelectric performance of a single material and that a device requires two semiconductor components, an n-type and

a p-type, to generate power, a ZT value representative of the couple was developed and is shown below.

$$ZT_{couple} = \frac{\left(\alpha_p - \alpha_n\right)^2 T}{(\rho_n \kappa_n)^{\frac{1}{2}} + (\rho_p \kappa_p)^{\frac{1}{2}}} \quad (2)$$

Here all of the same variables from equation 1 are present, except that those denoted with a "p" or "n" subscript are associated with the p-type and n-type component material properties, respectively[2]. The efficiency of a thermoelectric device is effectively limited by the Carnot efficiency ($\Delta T/T_H$), where the device efficiency ($\eta$) is related to the power input to the external load (W) and the net heat flow ($Q_H$), as seen below:

$$\eta = \frac{W}{Q_H} = \frac{T_H - T_C}{T_H}\left[\frac{(1+ZT_M)^{\frac{1}{2}} - 1}{(1+ZT_M)^{\frac{1}{2}} + \frac{T_C}{T_H}}\right] \quad (3)$$

Equation 3 above also relates the device efficiency to the ZT of the device couple, where $T_H$ and $T_C$ are the temperatures of the hot and cold sides, respectively, and $ZT_M$ is the device ZT at the average temperature[2,4,5]. This relation shows that the device efficiency is proportional to $(1+ZT_M)^{1/2}$, and that the device efficiency approaches the Carnot efficiency ($[T_H-T_C]/T_H$) as $ZT_M$ reaches infinity, which illustrates the importance of maximizing the device ZT. However, the practical limit for ZT for decades has been considered to be between 1 and 2.

## B. Material Requirements

### 1. Electronic Requirements

As shown in equation 1, thermoelectric performance is directly related to high electrical properties; thermopower and electrical conductivity. The product of the two, as $\alpha^2\sigma$, is referred to as the power factor, and as this factor is in the numerator of the ZT

equation, maximizing this term boosts thermoelectric performance. Electrical conduction through a material is calculated using the following equation:

$$\sigma = e \cdot n \cdot \mu \tag{4}$$

where e is the elementary charge ($1.602 \times 10^{-19}$ C), n is the concentration of charge carriers participating in conduction ($m^{-3}$), and μ is the mobility of the charge carrier ($m^2/V \cdot s$). Metals intrinsically possess high carrier concentrations and mobilities, providing them with a high electrical conductivity. Semiconductors on the other hand lack the high intrinsic carrier concentrations of metals, and therefore rely on increasing the concentration through thermal generation or carrier doping. Additionally, the carrier mobility in semiconductors is lower than metals, and combined with lower carrier concentrations results in lower electrical conductivity.

An advantage which semiconductors have over metals with regard to thermoelectric properties, though, is that the Seebeck coefficients are generally higher. However, the relationship between and electrical conductivity and Seebeck coefficient is somewhat reciprocal in nature. First off, the Seebeck coefficient is the potential generated through a thermal gradient. Since the potential generated is a result of the migration of charge carriers from cold to hot (low energy to high energy), Seebeck coefficient can be thought of, simply, as the "heat" energy per carrier over temperature or the entropy per carrier[6]. Therefore, with a fixed amount of "heat" energy available, an increase in the total number of charge carriers (concentration) would in essence "dilute" the amount of energy per carrier, thereby leading to lower thermopower. It is because of this inverse relationship that efforts to increase electrical conductivity, to improve thermoelectric performance, through the addition of charge carriers through doping is usually met with a corresponding decrease in thermopower, which hinders the potential gains in the power factor overall.

## 2. Thermal Requirements

Thermoelectric performance is inversely proportional to thermal conductivity (equation 1), and therefore low thermal conductivity in a thermoelectric materials is

desirable. Metals, for example, show very high electrical performance but very high thermal conductivity, resulting in poor thermoelectric performance. Thermal transport in a crystal lattice is a combination of contributions from charge carriers (electrons and holes) and lattice vibrations, known as phonons. The total thermal conductivity of a materials is therefore represented as $\kappa = \kappa_E + \kappa_L$, where $\kappa_E$ and $\kappa_L$ are the electronic and lattice contributions, respectively. Using the Wiedemann-Franz Law, the electronic contribution to thermal conductivity can be determined using the equation below[7]:

$$\kappa_E = \sigma \cdot L_0 \cdot T \tag{5}$$

where σ is the electrical conductivity (Ω·m), $L_0$ is the Lorenz number ( $\frac{\pi^2}{3}\left(\frac{k_B}{e}\right)^2 = 2.44\text{x}10^{-8}$ $\text{W}\cdot\Omega\cdot\text{K}^{-2}$), and T is temperature (K). The lattice contribution to thermal conductivity is determined through the relation below.

$$\kappa_L = \frac{1}{3} C_p \cdot v \cdot l_{ph} \tag{6}$$

where $C_p$ is the heat capacity of the material, v is the lattice velocity, and $l_{ph}$ is the phonon mean free path through the lattice. In general the lattice velocity can be expected to be relatively constant with temperature. Therefore the dominant factors in lattice conductivity are the temperature dependent heat capacity and the phonon mean free path.

In oxide semiconductors, since the carrier concentrations are low, lattice thermal conductivity becomes the dominant contribution to overall thermal conductivity. Therefore, research into reducing the thermal conductivity of these materials has focused predominantly on reducing the lattice contribution through phonon mean free path disruption. This has been accomplished through a variety of means, such as using point defects (solid solutions and "rattling" cage structures)[3] and planar defects (Magnèli phases and layered structures)[8,9].

## C. Current Promising Thermoelectric Materials

Historically, conventional TEGs have been composed of couples made from metallic compounds, such as bismuth telluride. In recent years, though, more interest has been shown in researching oxide materials as potential thermoelectric materials since the discovery of good thermoelectric performance in sodium cobaltite and strontium titanates. Additionally, oxides can have advantages over other thermoelectric materials if they are composed of elements that are abundantly available, are non-toxic, and have good chemical stability in air at high temperatures[9].

In general it is difficult to control and improve certain thermoelectric properties without diminishing others. For example, a typical method for improving thermoelectric performance is by increasing the electrical conductivity through carrier doping. However, an increase in the carrier concentration will increase the electronic contribution to thermal conductivity, possibly diminishing some benefits to ZT that would have been gained with an increase in power factor. On the other hand, efforts to reduce thermal conductivity using scattering interfaces can also interfere with charge carrier transport through the crystal, reducing mobility and overall electrical conductivity. Therefore, great interest has been placed on pursuing methods for effectively decoupling the thermal and electrical properties of thermoelectric materials.

### 1. PGEC and Hybrid Crystal Structures

Slack[10] proposed the idea of researching thermoelectric materials that behave thermally and electronically as a "phonon-glass/ electron-crystal" (PGEC). Essentially, this concept states that the best thermoelectric performance would be obtained with a material that shows phonon transport similar to glasses and the electronic transport of single crystal. Such a material would have the mean free path of phonons as short as possible (maximum scattering), while the mean free path of the charge carriers (electrons or holes) as long as possible (minimum scattering).

Koumoto et. al.[9] discussed the effectiveness of the PGEC concept to manipulate thermoelectric performance, and refers to the engineering of such materials as "nanoblock integration" and results in the formation of a "hybrid crystal." The hybrid

crystal is effectively a composite material, where there are multiple "nanoblocks," or subunits possessing different chemistries or structures, layered together to form a superstructure. Given their different characteristics relative to one another, each nanoblock contributes different properties to the overall material. A schematic drawing of a hybrid crystal is shown in Figure 2. In this drawing, nanoblock A possesses high thermopower while nanoblock B possesses low thermal conductivity. Therefore, the hybrid crystal constructed of layers of such subunits would in theory be able to maximize electrical performance while minimizing thermal conduction, thereby maximizing the figure of merit ZT. In fact, the strontium titanate Ruddlesden-Popper phases and the sodium/calcium cobaltite materials demonstrate this concept with their layered structures.

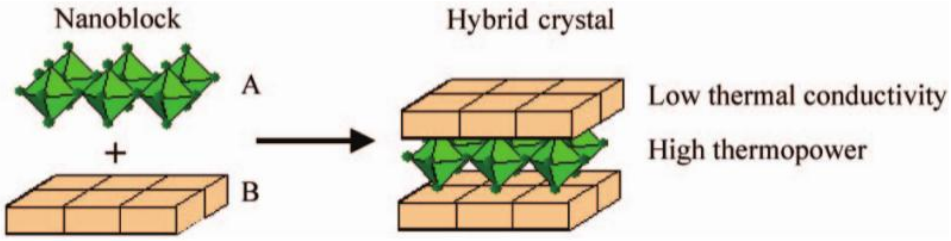


Figure 2. Schematic drawing of the assembly of a "hybrid crystal"[9].

a. Strontium Titinate Ruddlesden-Popper Phases

Strontium titanate (STO) has been researched extensively over the past decades as a potential thermoelectric material due to its promising n-type thermoelectric properties stemming from its high electrical performance. STO has a perovskite crystal structure which has shown to be structurally favorable towards substitutional doping, allowing for further improvements in electrical properties. Additionally, the high effective mass of the electrons in these materials allows for not only a high thermopower output, but also for the material to sustain its high thermopower over a large temperature range. Overall, the power factors of STO materials are comparable to that of conventional bismuth telluride thermoelectrics. However, as a result of the simple nature of the perovskite structure, STO shows high lattice thermal conductivity resulting from a lack of structural components responsible for phonon scattering. This high lattice thermal conductivity has

been detrimental to its thermoelectric performance overall[9,11,12]. The highest reported ZT for STO is 0.37 at 1000 K, from a thin film sample of 20 at% Nb-doped STO[13]. The same composition in polycrystalline form yielded a ZT of only 0.35 at 1000 K[14]. Both values, although very high for a thermoelectric material, are unfortunately not high enough for STO to be used in a TEG device (ZT>1).

Overall, the effects of solid solutions and alloying have shown limited effectiveness in reducing the lattice thermal conductivity in STO. As such, other methods for improving the thermoelectric performance of oxide materials through the reduction of lattice thermal conductivity such as engineering hybrid structures have been investigated. In 1957 Ruddlesden and Popper[15] determined the structure of $Sr_3Ti_2O_7$. This structure is one of many in a homologous series, chemically written as $SrO(SrTiO_3)_n$ (n=integer), now referred to as Ruddlesden-Popper (RP) phases, and involves the periodic block layering of SrO and $SrTiO_3$, both of the perovskite structure. In this homologous series $SrO(SrTiO_3)_n$, "n" denotes the number of $SrTiO_3$ blocks stacked between the individual layers of SrO, shown schematically in Figure 3[9,11]. It is generally agreed upon that in these phases the $SrTiO_3$ blocks are responsible for electron conduction, while the SrO layers act as electrically insulating barriers[16,17]. These STO-RP phases are regarded as natural superlattices (nanoblock integration), and are therefore expected to suppress the mean free path of phonons travelling through the sample through scattering at the layer interfaces.

Koumoto et. al.[9] compared the thermoelectric properties of polycrystalline Nb:STO and the STO-RP (n=2) called "STO-327." Both samples possessed similar charge carrier concentrations, but the electrical conductivity of the STO-327 was slightly higher and the thermopower slightly lower. The thermopower differences were attributed to differences in electron effective mass. At 300 K, the thermal conductivity of the STO-327 RP sample was roughly half that of the Nb:STO sample. This suggests that the presence of this layered structure, forming effectively a hybrid crystal, does in fact lead to a significant increase in phonon scattering.

In another study, Koumoto et. al.[11] studied the differences in thermoelectric performance of STO and 5%Nb-doped STO-$RP_2$ ("$RP_2$" means n=2). They found that there was a 60% reduction in thermal conductivity, predominantly due to diminished

lattice contributions, at room temperature and a 30% reduction at 1000 K when comparing the STO-RP sample to STO. This translated to a ZT of 0.14 at 1000 K for the 5%Nb:STO-$RP_2$ sample, which is less than half of that found in 20%Nb:STO (ZT of 0.37). Although the overall thermoelectric performance of these hybrid crystal materials is still too low for commercial applications, these materials stand as a proof of concept that significant reductions in thermal conductivity can be achieved when layering such as this is incorporated into the crystal structures.

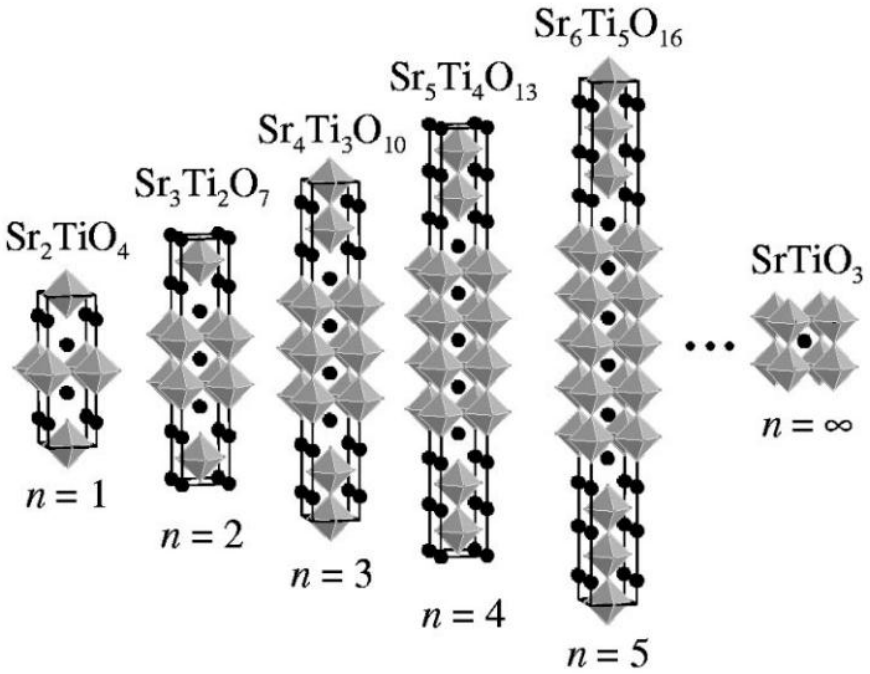


Figure 3. Crystal structure schematics of $SrO(SrTiO_3)_n$ (n=1-5) Ruddlesden-Popper homologous series[18].

b. Calcium Cobaltite Layered Structure

In 1997 Terasaki et. al.[19] reported promising thermoelectric properties in single crystals of $\gamma$-$Na_xCoO_2$ (x=0.7), another layered structure. Since then, there has been much research into the thermoelectric properties of similar layered structures, most notably those in the calcium cobaltite system. $\gamma$-$Na_xCoO_2$ is a hybrid structures and possess layers of triangular $CoO_2$ ($CdI_2$-type) as nanoblocks. Between each layer of $CoO_2$

is a nanoblock of $Na^+$ ions. The strongly correlated electronic structure of the $CoO_2$ layers provide the primary pathway for electronic conduction through the crystal, while the loosely bound sodium ion layer and its interfaces act as strong phonon scattering locations. However, one serious problem with $\gamma$-$Na_xCoO_2$ regarding thermoelectric performance is the diffusion of the $Na_+$ ions at high temperatures, which degrades the favorable properties[9,20].

The calcium cobaltite compounds can also form hybrid crystals, and the most notable of these is $Ca_3Co_4O_9$. These compounds can be written as $(Ca_2CoO_3)_pCoO_2$, where p is the b-axis ratio ($b_{CoO2}/b_{Ca2CoO3}$). Different from $\gamma$-$Na_xCoO_2$, these calcium cobaltites have square blocks of $Ca_2CoO_3$, of the NaCl-type, between the triangular $CoO_2$ layers instead of sodium atoms, seen in Figure 4. The result is a "hexagon-on-square" structure which is highly distorted with the misfit between the nanoblocks along the b-axis. Similar to the sodium ion nanoblock, the presence of these $Ca_2CoO_3$ layers increase phonon scattering through the crystal[9,20].

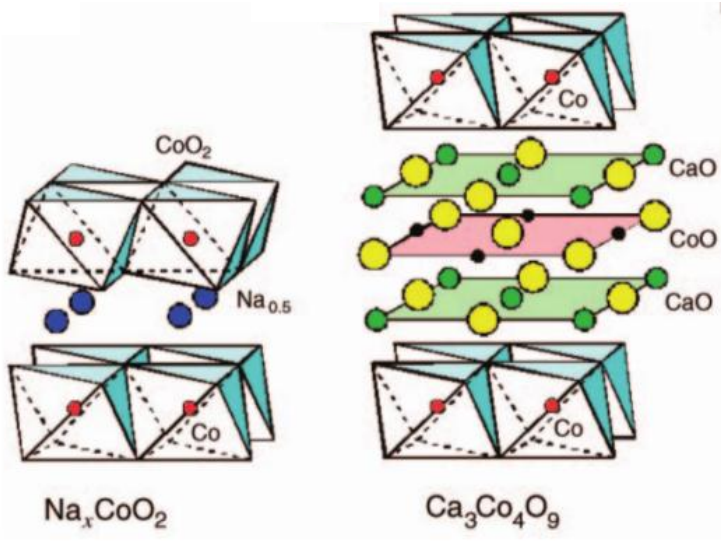


Figure 4. Schematic drawing of the hybrid crystal structures of $Na_xCoO_2$ and $Ca_3Co_4O_9$[9].

With regard to thermoelectric properties, both $\gamma$-$Na_xCoO_2$ and $Ca_3CoO_3$ show high p-type thermopower, even at high temperatures, which is attributed to the low-spin

states of both the $Co^{3+}$ and $Co^{4+}$ ions in the $CoO_2$ conduction layer. Miyazaki[20] tested the thermoelectric properties of $Na_{0.70}CoO_2$ and $[Ca_2CoO_3]_{0.62}CoO_2$. Both samples showed metallic-type electrical resistivity with temperature. However, the $[Ca_2CoO_3]_{0.62}CoO_2$ sample showed 5 times greater resistivity compared to $Na_{0.70}CoO_2$, but with a 1.6 times greater thermopower and 30% smaller (~1 W/m·K) thermal conductivity at 300 K. Overall, the ZT was ~0.035 for both samples at 300 K, which is attributed to high resistivity in both samples. It is for this reason that many researchers have been investigating methods to improve the electrical properties of these samples, especially $Ca_3Co_4O_9$, through substitutional doping of Co. Chromium additions have shown a 25% increase in power factor[21], titanium a 55% increase[22], and sodium a 70% increase[23], all at 800 °C. Regardless of the thermoelectric performance overall these structures demonstrate that the presence of layered structures (hybrid crystals) result in an increase in phonon scattering, thereby significantly reducing lattice thermal conductivity.

## 2. Crystallographic Shear Planes: $TiO_2$ Magnèli Phases

When oxygen is removed from the $TiO_2$ rutile structure, the formation of what are known as Magnèli phases is possible. These phases form a homologous series, following the chemical formula $Ti_nO_{2n-1}$ (n=integer), and are composed of the rutile base structure with a periodically spaced arrangement of dense planar defects resulting from oxygen deficiency. These planar defects are referred to as crystallographic shear structures[8]. In addition to the titanium-oxygen system, Magnèli phases have also been confirmed in the tungsten-oxygen, molybdenum-oxygen, and niobium-oxygen systems[24]. A Magnèli phase is derived from the rutile structure as follows[8,25]:

a) A shear plane is a crystallographic plane to which the rutile structure is periodically divided into blocks along parallel planes;
b) These blocks are then translated along the shear vector relative to each other; and,
c) Any overlapping parts generated through the translations are removed.

In the $Ti_nO_{2n-1}$ Magnèli phases, when n=1-10 the crystallographic shear plane (CSP) is the $(121)_{rutile}$ and is sheared along the $\frac{1}{2}[0\bar{1}1]_{rutile}$ vector[26,27]. When n>10, the shear vector changes to $(1\bar{3}2)_{rutile}$[24,28]. Given the relative positions of other oxygen atoms

along this shear vector, the translation does not result in any disturbance in the oxygen sublattice. However, the translation along this shear vector results in the movement of the titanium atoms within the [$TiO_6$] octahedra into interstitial octahedral positions, resulting in a disturbance in the structure along the crystallographic shear planes. A drawing of the crystallographic shear planes within the $Ti_6O_{11}$ Magnèli phase (n=6) is shown in Figure 5, where the distortion among the titanium atoms along the planes is visually evident. The spacing between the periodically spaced shear planes is a function of the oxygen deficiency of the lattice, where the spacing decreases as oxygen deficiency increases[8].

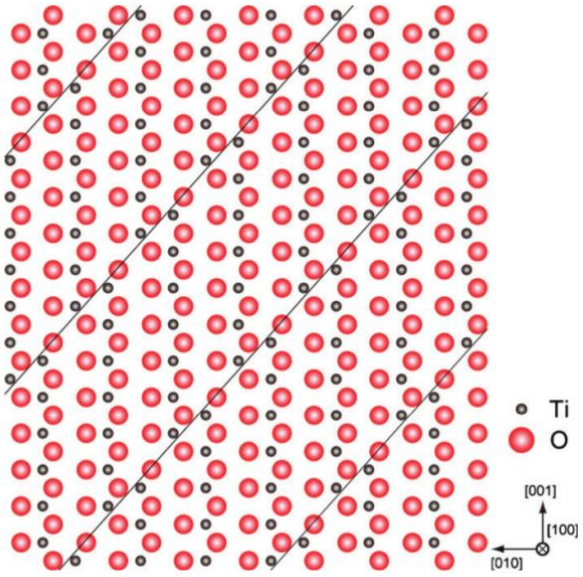


Figure 5. Projection along the x-axis of the $Ti_6O_{11}$ Magnèli phase (n=6), showing the crystallographic shear planes along the $(121)_{rutile}$ planes[8].

Given that one method for increasing thermoelectric performance in materials is to reduce the lattice thermal conductivity, these Magnèli phases have been investigated to determine the extent to which this can be achieved as a result of the presence of the CSPs. Harada et. al.[8] investigated the thermoelectric properties of hot-pressed, polycrystalline $TiO_{2-x}$ (x=0.05, 0.10, 0.15, and 0.20). In general all samples were n-type and showed metallic conduction. Additionally, electrical conductivity increased with decreasing oxygen content, indicating that the CSPs do not impact electrical conduction negatively

through carrier scattering. Seebeck coefficient decreased with oxygen deficiency, though this behavior is predictable given the expected increase in carrier concentration with increased substoichiometry.

Overall, lattice thermal conductivity decreases with decreasing oxygen content, and the $Ti_4O_7$ sample, for example, shows 60% and 40% reductions in thermal conductivity at 300 K and 773 K, respectively, when compared to stoichiometric, polycrystalline $TiO_2$ (of similar grain size). The authors used the Debye model to determine the mean free path of the phonons at room temperature to be 0.8 nm, which is comparable to the estimated spacing between the CSPs of the Magnèli phases tested, being 0.5-2.0 nm. Therefore, it was concluded that the reduction in lattice thermal conductivity is directly related to phonon scattering at the crystallographic shear planes in the $TiO_2$ Magnèli phases.

### D. Beta-Gallia Rutile Intergrowth Structure

In 1972 Gibbs and Anderson reported the electron microscopy characterization of a homologous series of structures in the $Ga_2O_3$-$TiO_2$ binary system, following the chemical formula $Ga_4Ti_{n-4}O_{2n-2}$ ($15 \leq n \leq 23$, odd)[29]. Since then, the homologous series has been expanded to include the phases where $15 \leq n \leq 31$[30]. Using electron diffraction contrast analysis, the structures were derived from the rutile structure with periodic displacement boundaries parallel to the $(210)_{rutile}$ planes. These boundaries were found to contain elements of β-$Ga_2O_3$ that were coherently grown into the rutile structure, and the resulting phase is referred to as a beta-gallia rutile intergrowth (BGR). Similar to the Magnèli phases, the BGR intergrowths are referred to as a kind of crystallographic shear plane (CSP). A schematic drawing of the $Ga_4Ti_{21}O_{48}$ (n=25) is shown in Figure 6, where the β-gallia structure elements are shown in yellow. The indexed structural data used to construct Figure 5 was taken from work done by Lloyd et. al.[31] using the monoclinic space group C2/m.

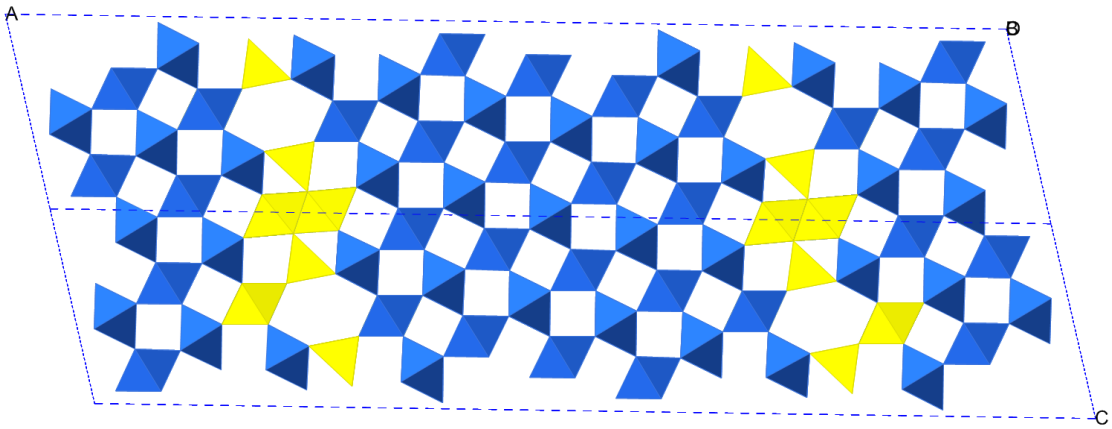


Figure 6. Schematic drawing of BRG structure, n=25[31], with the [$TiO_6$] octahedra in blue and the β-gallia elements in yellow.

The BGR structure, as described above, can be thought of as rows of β-gallia placed periodically between slabs of rutile along the $(210)_{rutile}$ plane. In the monoclinic β-$Ga_2O_3$ structure, gallium atoms are both tetrahedrally and octahedrally coordinated. The octahedra are edge sharing and link together to create chains. The tetrahedra are connected by corner sharing, and share corners with the chains of octahedra, giving the structure a columnar quality. The rutile $TiO_2$ structure is described more simply as just the corner sharing of [$TiO_6$] octahedra. Therefore, the BGR structure can be described as having columnar sections of the β-$Ga_2O_3$ structure placed at the $(210)_{rutile}$ displacement boundary, whereby, relative to the conventional x y z crystal coordinate system, the gallia structures are rotated by 180° and expanded slightly. Additionally, the rutile structure blocks are translated at the $(210)_{rutile}$ boundary along the [½¼½] displacement vector. The rotation of the β-$Ga_2O_3$ elements is required to match the rutile and gallia oxygen sublattice sites, and results in the formation of the large tunnels within the BGR structures, spaced 10.3 Å apart and 2.5 Å in diameter[31-33].

The boundary between the β-$Ga_2O_3$ and the rutile within the BGR structure can be described as a "zig-zag," or saw-tooth-like shape, where the edge sharing octahedra that are parallel to [001] are joined through corner sharing to the tetrahedra. Analysis of the bond lengths of the octahedral chains within the β-$Ga_2O_3$ structural elements revealed that these sites have a mixed sharing of 64 Ga to 36 Ti[31,33]. Therefore, given the extensive

distortion along these $(210)_{rutile}$ displacement boundaries and the presence of two chemically distinct blocks (β-$Ga_2O_3$ and rutile), this author hypothesizes that the presence of these structures within the rutile lattice will result in an increase in phonon scattering, and therefore a decrease in thermal conductivity similar to the STO-RP phases, $Ca_3Co_4O_9$, and $TiO_2$ Magnèli phases. This, in turn, could result in favorable thermoelectric properties. Additionally, since the distance between the intergrowths is a function of composition, similar to the other referenced layered systems, where the distance decreases with decreasing titanium to gallium ratio (or simply n-value), it is further hypothesized that thermal conductivity will decrease as n-value decreases.

## E. Synthesis Methods

### 1. Solid-state Synthesis

Prior to this and related work, β-gallia rutile intergrowths have only been prepared in bulk using solid-state synthesis[29-36]. Solid-state synthesis involves a mixture of solid precursors, and in the case of the present work, oxides. High temperatures in excess of 1000 °C are required to drive the reaction. There are both thermodynamic and kinetic factors which control solid-state reactions. The thermodynamic factors relate to the formation of phases based on changes in free energy (the formation of the BGR phase), and the kinetic factors determine the rate by which the reaction occurs, based on diffusion.

Figure 7 shows a phase diagram of the β-$Ga_2O_3$-$TiO_2$ binary system, reported by Kamiya et. al.[30] From this diagram it can be concluded that all BGR compositions from n=15 through 31 are stable in air above 1335 °C. Therefore, heat treatments above this temperature will be required to form any BGR phase.

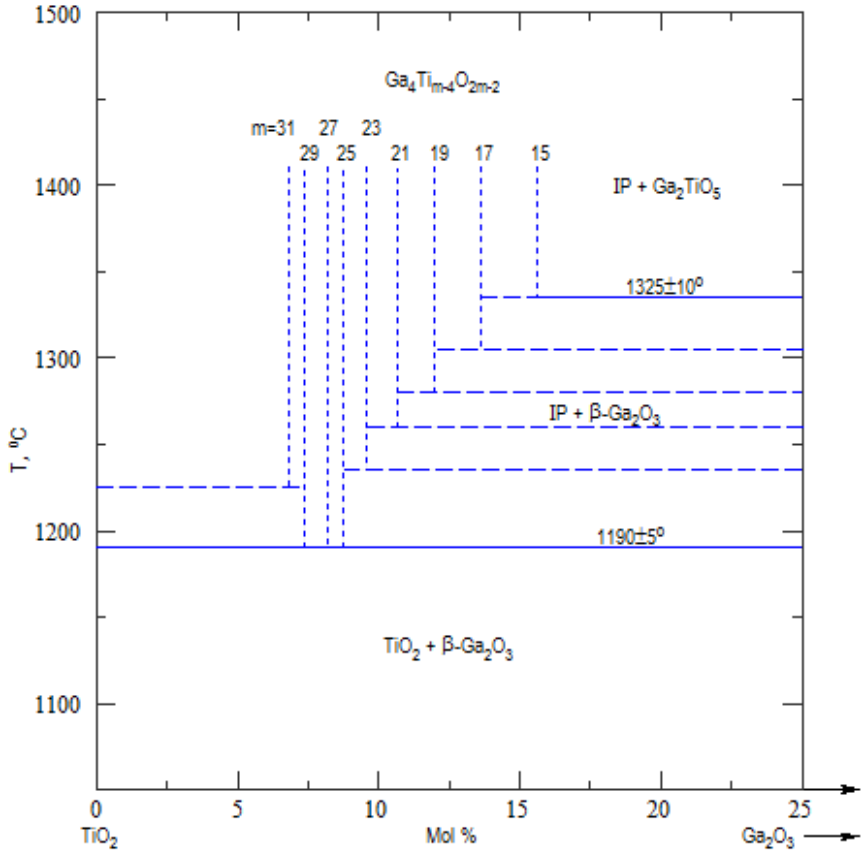


Figure 7. Phase diagram of the β-$Ga_2O_3$-$TiO_2$ BGR system[30].

## 2. Combustion Syntheiss

To the author's knowledge, prior to this and related work at Alfred University, solution combustion synthesis has never been used to prepare BGR. This synthesis method is advantageous over other methods, such as solid-state synthesis, as the precursors are all soluble in water. This allows for a better mixing of reactants, and therefore would improve chemical homogeneity of the final product. Additionally, combustion synthesis is a quick process, requiring only minutes from reaction start to completion, compared to the many days for conventional solid-state synthesis.

Combustion synthesis involves the controlled combustion of water soluble precursors, typically transition metal nitrates and a fuel, of which urea or carbohydrazide

are common[37,38]. The products of the reaction are an oxide powder and a mixture of gases; $CO_2$, $NO_x$, and ammonia. The synthesis of oxides is typically conducted in an open container at constant pressure (atmospheric). The combustion reaction is controlled using what is referred to as the elemental stoichiometric coefficient, which takes into account relative molar amounts of fuel and oxidizer precursors, seen below in Equation 7.

$$\Phi = \frac{\Sigma\, x_O \cdot v_O}{(-1)\Sigma\, x_F \cdot v_F} \tag{7}$$

Where Φ is the elemental stoichiometric coefficient, $x_O$ and $x_F$ are the mole fractions of the oxidizer and fuel precursors, respectively, and $v_O$ and $v_F$ are the redox valencies[39]. The adiabatic flame temperature of the combustion reaction increases as Φ approaches 1. Therefore reaction temperature can be controlled using Φ.

## F. Thermopower Analysis of a Polaron Conductor

Charge carrier conduction through a band conductor takes place within the conduction band, where electrons are not localized to any atoms and are therefore free to move throughout the lattice. Unlike band conduction, polaron conduction involves the migration of charge carriers from one localized site/atom to another, described as a hopping motion[40]. In n-type $TiO_2$, for example, an electron will "hop" from a $Ti^{3+}$ site to a $Ti^{4+}$ site, whereupon the $Ti^{4+}$ site becomes a $Ti^{3+}$[41]. In order for the electron to make the jump from site to site, it must overcome the localized binding energy of the $Ti^{3+}$ atom. This binding energy is referred to as the activation energy of hopping. Additionally, an electron can only hop to a vacant, adjacent $Ti^{4+}$ site. A $Ti^{4+}$ site is considered "vacant" because it can accept and localize an electron, and upon doing so becomes a $Ti^{3+}$ site, incapable of accepting any more electrons.

The temperature dependence of thermopower for a band conductor is described using the equation below[40]:

$$\alpha = \pm \frac{k_B}{e}\left(\frac{E_\alpha}{k_B T} + \frac{S_v}{k_B}\right) \tag{8}$$

where α is thermopower, $k_B$ is the Boltzmann constant, e is the elementary charge, $E_\alpha$ is the activation energy for carrier generation, T is temperature, and $S_v$ is the vibrational entropy of the lattice (which is assumed here to be negligible). The activation energy for carrier generation can be calculated from the slope of an Arrhenius plot of $\alpha \cdot (e/k_B)$ vs. 1/T. When thermopower is not dependent on temperature, the activation energy here is zero. This is an attribute associated with polaron conduction. Therefore, the expression used to model thermopower in a polaron conductor is given by the following equation[40]:

$$\alpha = \pm \frac{k_B}{e}\left[\ln\left(\beta \frac{1-c}{c}\right) + \frac{S_v}{k_B}\right] \tag{9}$$

where β is the spin degeneracy of $Ti^{3+}/Ti^{4+}$ (6) and c is the site fraction of $Ti^{3+}$. The temperature dependence of electrical conductivity is given by:

$$\sigma T = \sigma_0 \exp\left(\frac{E_\sigma}{k_B T}\right) \tag{10}$$

where σ is the electrical conductivity and $E_\sigma$ is the activation energy for conduction[42]. When the temperature dependent electrical conductivity is plotted as ln(σT) vs. 1/T, the activation energy can be extracted. Overall, the relationship between activation energy terms is as follows: $E_\sigma = E_\alpha + E_\mu$, where $E_\mu$ is the activation energy of mobility. In polaron conductors, $E_\mu$ is the activation energy of hopping and is effectively equal to $E_\sigma$ (as $E_\mu = E_\sigma - E_\alpha$ where $E_\alpha \sim 0$).

# II. EXPERIMENTAL PROCEDURE

## A. Synthesis Methods; Combustion and Solid-State

Solution combustion synthesis was used to prepare the BGR samples. The chemical precursors used for this work were gallium (III) nitrate hydrate (Puratronic 99.999%, #11150, Alfa Aesar, Ward Hill, MA, USA), dihydroxybis(ammonium lactato) titanium (IV) (50% w/w aq. solution, #42676, Alfa Aesar, Ward Hill, MA, USA), and ammonium nitrate (ACS, 95% min, #12363, Alfa Aesar, Ward Hill, MA, USA). This approach differs from typical combustion synthesis reactions in that the source of titanium is an organometallic complex which acts as a fuel and is balanced using ammonium nitrate. All precursors were mixed together in a Pyrex beaker with 35 mL of deionized water, to aid in dissolution, and each sample was batched to obtain a theoretical yield of 5 grams of BGR. The prepared solutions were added to a 1 L Pyrex beaker and placed in a furnace preheated to 500 °C, and remained in the furnace for a total of 14 minutes. All of the samples prepared in this work were synthesized using $\Phi = 0.5$; a fuel rich mixture. This coefficient was chosen because a coefficient closer to unity leads to a more energetic combustion reaction, resulting in a considerable loss of sample.

The powders resulting from combustion synthesis were fluffy nanopowders, as confirmed by SEM, agglomerated into large, cauliflower-like formations. Mortar and pestle was used to break up this agglomeration to produce the final powder product. At this stage in the synthesis process the powder samples showed anatase phase character, and required a high temperature heat treatment to form the beta-gallia rutile intergrowth phase. A platinum crucible was used as the heat treatment vessel, and the samples were ground with a mortar and pestle and placed into a furnace (air) preheated to 1000 °C. The furnace was heated to 1400 °C at 10 °C/min and held at temperature for 1 hour. Upon completion of the hour long dwell at 1400 °C, the samples were removed and quenched in air on a refractory plate. The resultant powders had consolidated into a loosely bound puck, which showed yellow coloration on the surface and white coloration in the bulk.

These sample pucks were ground and homogenized using mortar and pestle to produce the final BGR product.

A BRG sample (n=19) was also synthesized using solid-state synthesis. Measured amounts of gallium oxide (99.99+%, #215066, Sigma-Aldrich, St. Louis, MO) and titanium dioxide (anatase, ≥99%, -325 mesh, #248576, Sigma-Aldrich, St. Louis, MO) were combined by mortar and pestle, pressed into pellets, and heated in a furnace in air at 1450 °C for 4 days. Post-heat treatment, the sample was a fairly dense, sintered pellet. The sample was crushed in a steel die and ground using an agate mortar and pestle, pressed into a pellet, and heat treated again at 1450 °C for 3 days. Finally, the pellet was ground again using mortar and pestle to achieve the final BRG powder sample.

### B. Spark Plasma Sintering (SPS)

All samples studied in this work were sintered using spark plasma sintering (SPS), also known as PECS (Pulse Electric Current Sintering). This was accomplished using an FCT HP D 25 (FCT Systeme GmbH, Rauenstein, Germany) furnace with graphite dies and punches. The powder BGR samples were loaded into 18.75 mm diameter dies lined with graphite foil and sintered according to the following parameters: 100 MPa of pressure, 100 °C/min. heating rate, ~1300 °C dwell temperature (~1100 °C on the program-controlled front pyrometer), 3 min. dwell time at temperature, and a 100 °C/min. cooling rate. The resultant disk samples were ground using silicon carbide grit paper to remove the graphite foil remaining of the surface. The sintered samples were dark blue in color. Bulk sample density was measured using the Archimedes method, where the samples were equilibrated in water within a mechanical vacuum chamber for 3 hours prior to wet measurements.

### C. Characterization

Qualitative phase analysis was performed using a Bruker D8 Advance X-ray diffractometer (Bruker ASX, Inc., Madison, WI, USA), equipped with copper Kα radiation. All pre-sintered powder samples were loaded into a back-loaded sample holder

and measured from 5-70 °2θ with a step size of 0.02 °2θ, a dwell time of 1 s, with the sample stage rotating at 30 rpm. Post-sintered, ground powder samples were measured using the same parameters, but in these cases front loaded sample holders were used. DIFFRAC.EVA 4.0 (Bruker ASX, Inc., Madison, WI, USA) was used to qualitatively identify the phase composition of each sample.

A Quanta 200F Environmental Scanning Electron Microscope (FEI, Hillsboro, OR, USA) was used to analyze the powder morphology and sintered microstructures of the samples under study. To provide surfaces suitable for microstructural analysis, the samples were embedded in an epoxy mold and polished using sub-micron media. Etching of the polished surfaces was accomplished by submerging the samples in boiling sulfuric acid (#A298-212, Fisher Scientific, Hampton, NH, USA) for 3 hours.

## D. Property Measurement

### 1. D.C. Conductivity and Thermopower Measurements

Samples disks were first cut into bars (approximately 3 mm x 3.5 mm x 15 mm). Figure 8 show schematically how a bar sample is arranged with the various electrodes within the sample fixture. As seen in this figure, a sample is contacted at opposite ends with electrodes 1 and 4, consisting of an arrangement of the thermocouple, a gold plate, and platinum foil. Platinum wire (0.01 in. diameter) was wrapped around the bars approximately 5 mm from the ends of the sample and connected to thermocouples 2 and 3. R-type thermocouples (13% Rh/Pt, 0.01 in.) were used for all measurements.

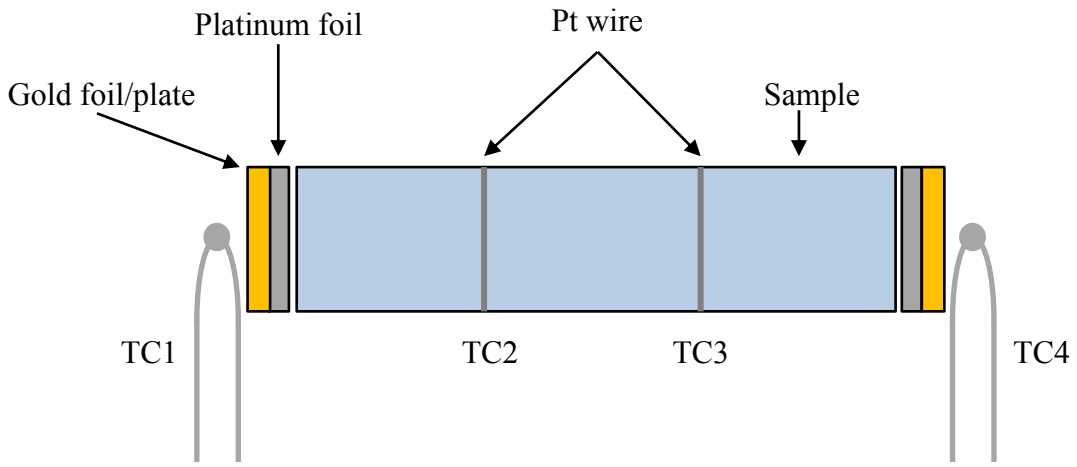


Figure 8. Schematic drawing of four-point combined DC conductivity/ thermopower measurement system fixture.

The in-house produced, LabVIEW (National Instruments Corp., Austin, TX, USA) controlled, simultaneous DC conductivity/thermopower measurement system uses a programmable current source (Model 2400 Sourcemeter, Keithley Instruments, USA) and voltage/current meter (Model 2700 Multimeter/Data Acquisition, Keithley Instruments, USA). The samples were measured using the following profile: from 100-1000 °C with heating rate of 5 °C/min and held at each temperature point for 5 minutes before measuring every minute for 5 minutes, resulting in a total of 95 individual data points. All samples were measured with 35 mA current source under flowing argon gas (~150 sccm). Thermopower data was measured between thermocouples 1 and 4, while D.C. conductivity was measured between thermocouples 2 and 3. A temperature dependent platinum correction factor for Seebeck coefficient was applied accordingly.

**2. Thermal Condutivity Measurements**

Sintered BRG sample were core-drilled to produce 12.7 mm x ~3 mm disks and coated with a thin layer of graphite using an aerosolized spray. Thermal conductivity measurements were conducted using an Anter Flashline 4010 (TA Instruments, New Castle, DE, USA), which employs the laser flash method. Samples were placed in aluminum oxide sample holders, and an aluminum oxide reference standard was used to simultaneously measure approximate heat capacity. Given that the laser flash method

directly measures the thermal diffusivity of a sample, thermal conductivity is related to diffusivity through Equation 11 below:

$$\kappa = \gamma \cdot \rho \cdot C_p \tag{11}$$

where κ is thermal conductivity (W/m·K), $\gamma$ is thermal diffusivity ($m^2/s$), ρ is bulk density ($Kg/m^3$), and $C_p$ is heat capacity (J/kg·K).

# III. RESULTS AND DISCUSSION

## A. Qualitative Phase Analysis and Phase Stability

### 1. Post Heat Treatment/Pre-sintering

The powder samples resulting directly from combustion synthesis are very fine and loosely agglomerated, showing sub-micron crystallite sizes (Figure 9a). X-ray diffraction experiments confirm the nano-scale nature of the powder crystallites, with significant peak line broadening observed. All as-synthesized BGR samples show only the anatase $TiO_2$ phase. The SEM micrographs shown in Figure 9 shows the dramatic change in grain morphology post-heat treatment in air at 1400 °C for 1 hour. In fact, a layered grain structure is noticeable in the heat treated powders, indicating the likely formation of the beta-gallia rutile intergrowth structure.

Powder X-ray diffraction was used to determine the phase composition of the combustion synthesized, heat treated BGR samples, shown in Figure 10. Compared to the as-synthesized samples, all heat treated samples showed complete phase transformation from anatase into other phases, predominantly BGR. Figure 11 shows that the combustion-synthesized n=25 sample matches well with regard to peak locations compared to the experimental diffraction data collected by Lloyd et. al.[31]. However, given that the only experimental diffraction data available on BGRs in the ICDD database is for the aforementioned n=25 sample and that the peak locations are expected to change with changes in BGR composition, direct phase identification is difficult. Therefore, it is assumed that all of the diffraction peaks seen in Figure 10 not labeled are attributed to the intergrowth phase. As such, immediately apparent in Figure 10 are the minor amounts of $\beta$-$Ga_2O_3$ present in the n=15 sample and rutile $TiO_2$ in all samples except n=19. This indicates that the compositional boundary of BGR phase stability under the processing conditions used, 1 hr. 1400 °C heat treatment with a quench in air, lies between n=17 and n=21.

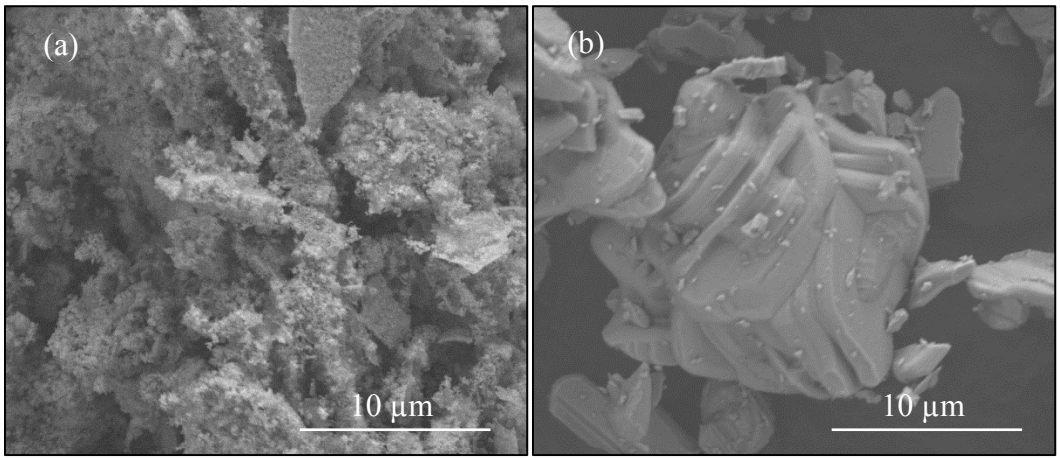


Figure 9. SEM micrographs (5,000X) of BGR (a) combustion synthesized nanopowders (as-synthesized) and (b) heat treated at 1400 °C for 1 hr.

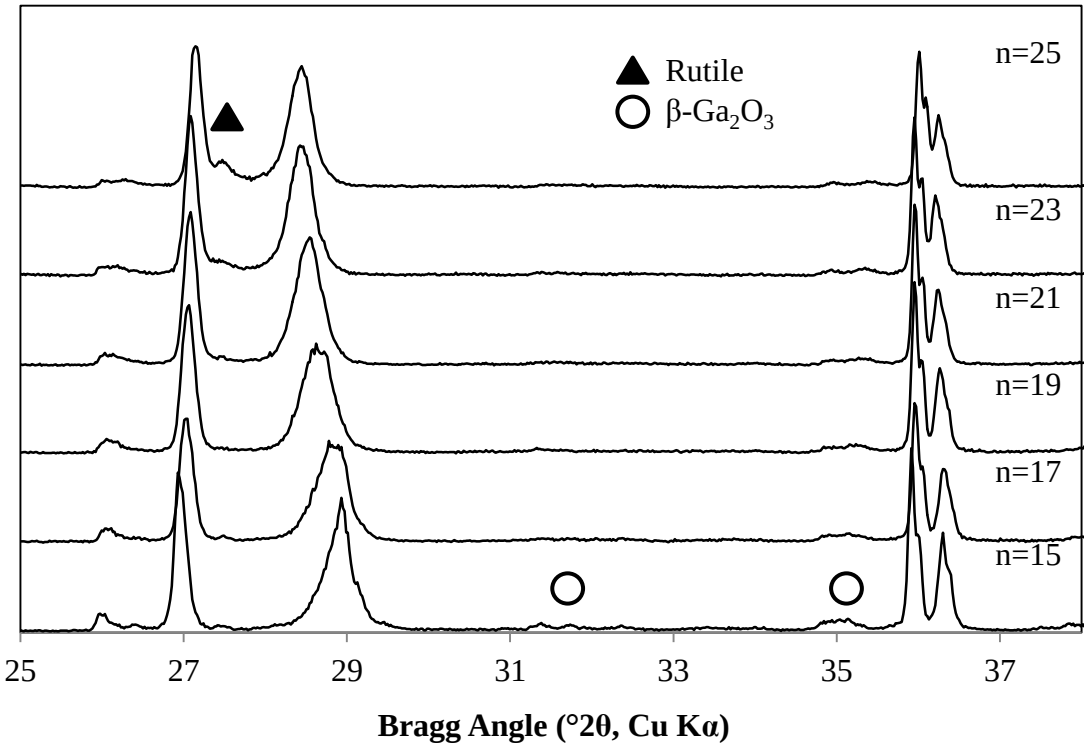


Figure 10. Powder XRD patterns of C.S. BRG samples after heat treatment at 1400 °C, air quenched.

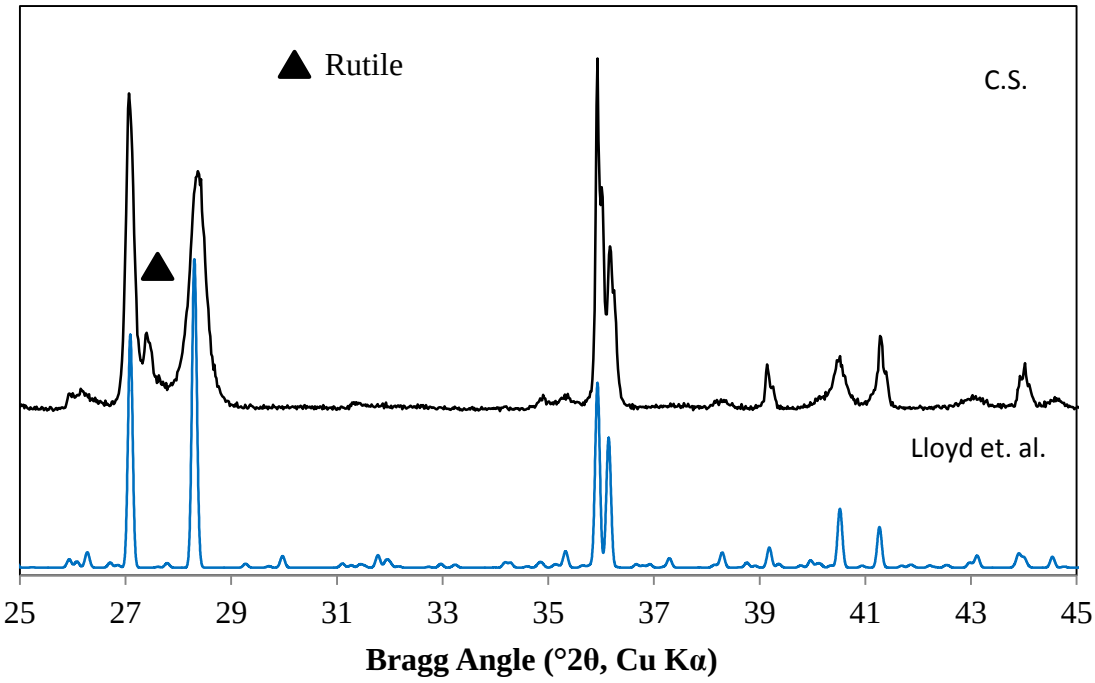


Figure 11. n=25 C.S. versus calculated pattern of BGR n=25 from experimental measurements conducted by Lloyd et. al.[31].

Figure 12 shows an overlay of the powder diffraction patterns of n=19 prepared using both combustion and solid-state syntheses. It is evident from this overlay that the BGR peak locations from both samples match fairly well, indicating that both synthesis methods yield crystallographically the same materials, with compositions consistent with the batch calculations. However, the peak shapes differ, with the C.S. sample showing significant broadening and asymmetry. This broadening and asymmetry here is thought to be due to the presence of a distribution of BRG phases compositionally similar to the intended compositions. For example, in this n=19 sample there are likely minor amounts of n=17 and n=23 present. If this idea is correct, it is possible that the processing parameters used were not adequate to reach equilibrium and phase uniformity. It is therefore possible that a longer heat treatment, exceeding 1 hr. (possibly extended into days like the S.S. sample), could result in a more uniform phase composition. However, there may be a limit to the extent of phase "uniformity" realistically achievable in the BGR system, as Lloyd et. al.[31] reported that amongst the bulk of their n=25 BGR sample

was a minor phase of n=23. The heat treatment of 1600 °C for 16 hours in oxygen with a rapid quench in air that they used was not sufficient to obtain a uniform n=25 phase.

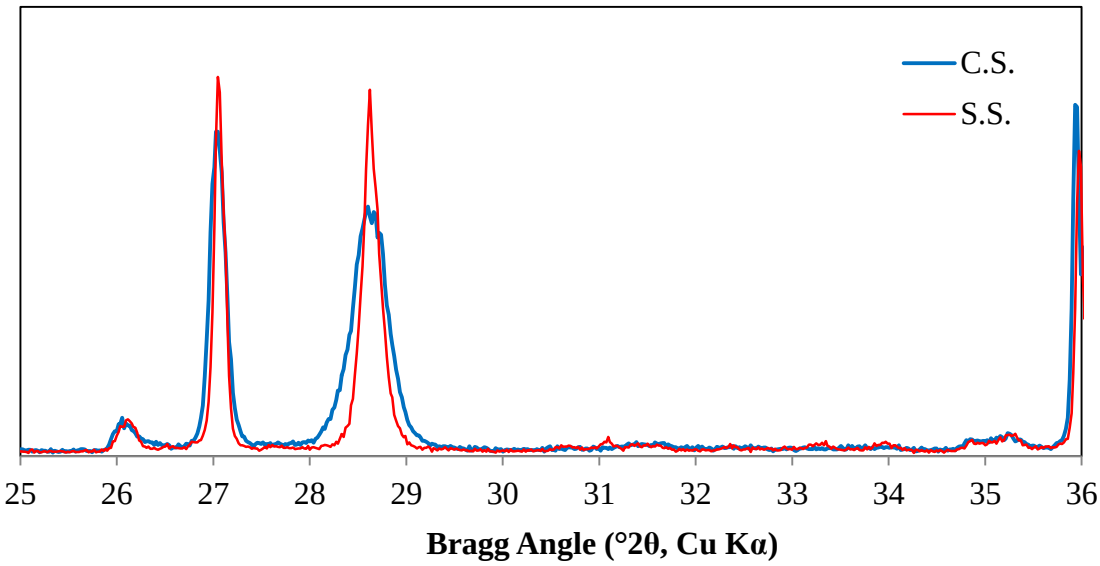


Figure 12. Powder XRD patterns of C.S. and S.S. n=19 samples.

Also evident in Figure 10 is that there is a decrease in the spacing between the two main X-ray diffraction peaks, at ~27 and 29 °2θ, with increasing n-value. Using Bragg's law ($\lambda = 2d_{hkl} \sin\theta$), the *d*-spacing corresponding to each peak were calculated, and the difference between the *d*-spacing of the two peaks determined and plotted as a function of compositions in Figure 13. The trend here shows a near linear relationship between a decreasing difference in *d*-spacing ($\Delta d$) and increasing n-value, and follows closely both in trend and magnitude with the work done by Jaromin et. al.[36]. The slightly lower $\Delta d$ of the Lloyd et. al. sample compared to the n=25 C.S. is attributed to the minor amount of rutile present in the C.S. sample, resulting in a lower n-value intergrowth phase present. This lower $\Delta d$ further supports the hypothesis that there is a linear relationship between $\Delta d$ and n-value, as a more linear trend can be seen in the data if the n=25 C.S. point was replaced with the Lloyd et. al. point. Overall, since there is no significant deviation from this trend among any synthesized samples, it is concluded that the difference in intended n-value composition is minimal. This, however, is under the

assumption that the minor amount of rutile present in some samples is not contributing significantly to the overall intergrowth composition.

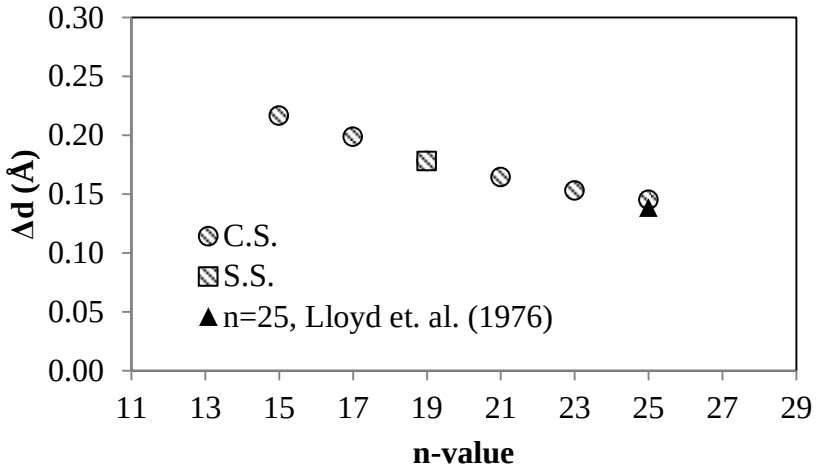


Figure 13. Difference in *d*-spacing (Δd) between twin peaks (~27 and 29 °2θ) vs. composition of BRG samples after heat treatment at 1400 °C, air-quenched, both C.S. and S.S. (error bars within data markers).

**2. Post-Sintering**

Spark plasma sintering was used to consolidate and sinter all BGR samples in this work, and through the chosen sintering parameters, ~1300 °C maximum temperature held for 3 minutes under 50 MPa of pressure, yielded samples exhibiting highly dense microstructures with less than 4% apparent porosity, seen in Table 1. In contrast with the sample sintered from S.S.-prepared powders, the C.S. samples showed significantly less apparent porosity; all compositions with less than 0.15%. The results of a scanning electron microscopy (SEM) study of the sample microstructures (Figure 14(a-d)), S.S. and C.S., concurs with these Archimedes density differences, showing levels of closed porosity roughly proportional to that of the measured apparent porosity.

It is likely that density differences are a result of powder particle size differences between the two synthesis methods; the powder resulting from solid-state synthesis is noticeably coarser than those prepared via combustion synthesis. This is evidenced by the difference in sintered grain sizes between the C.S. and S.S. samples, with the S.S. sample showing larger grain sizes, up to ~50 μm, compared with the up to ~30 μm grains of the

C.S. samples. The C.S. samples also show a comparatively larger fraction of smaller grains, below roughly 10 μm, which would have aided in densification. Figures Figure 14b and Figure 14d also show the presence of the layered intergrowth structure, with lines of compositional variation aligned differently relative to neighboring grains (random grain orientation). The bright dots in Figure 14d are suspected to be contamination during sample preparation.

Table 1. Archimedes Density Measurement Results for All Sintered BRG Samples

| Sample | | Bulk Density ($g/cm^3$) | Apparent Porosity (%) |
|---|---|---|---|
| C.S. | n=15 | 4.40 | < 0.15 |
| | n=17 | 4.38 | < 0.15 |
| | n=19 | 4.36 | < 0.15 |
| | n=21 | 4.36 | < 0.15 |
| | n=23 | 4.34 | < 0.15 |
| | n=25 | 4.33 | < 0.15 |
| S.S | n=19 | 4.12 | 3.15 ± 0.05 |

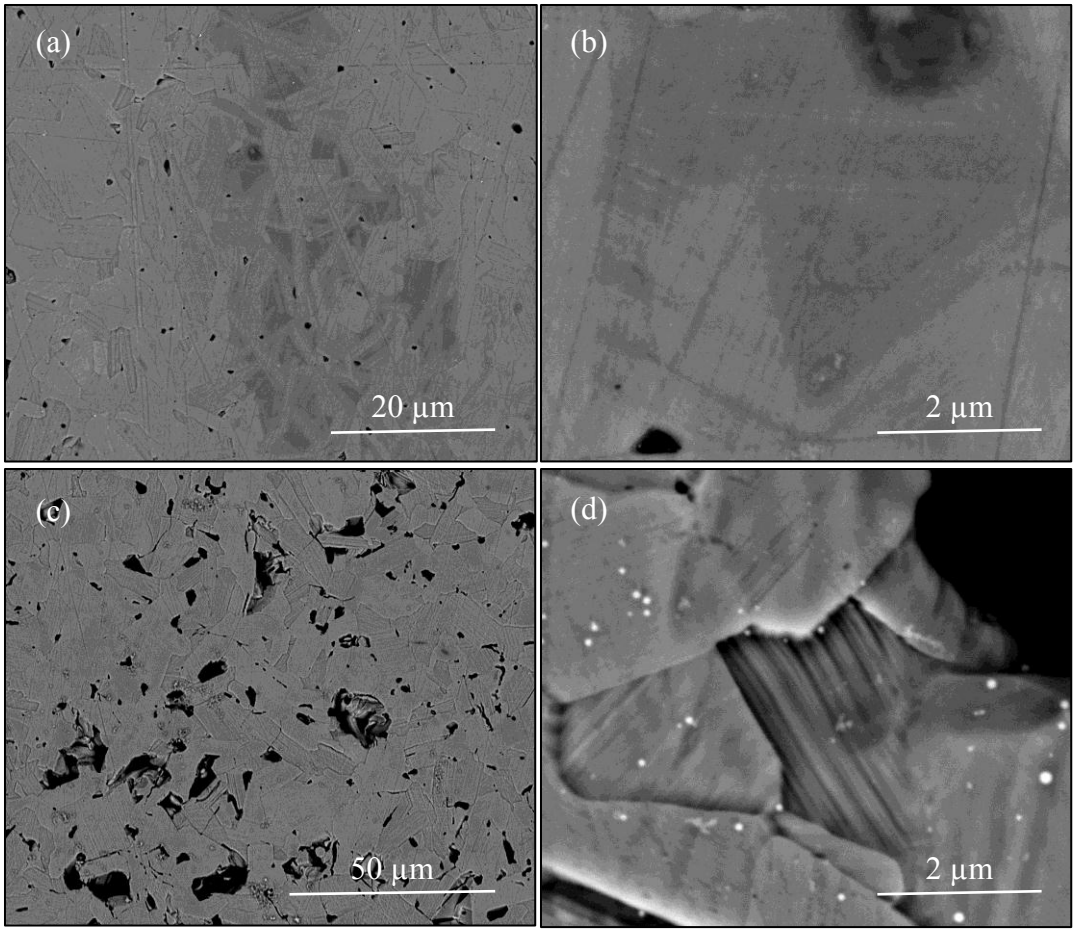


Figure 14. Back-scattered SEM micrographs of sintered (a) n=19 C.S. (2,000x), (b) n=19 C.S. (20,000x), (c) n=19 S.S. (1,000x), and (d) n=19 S.S. (20,000x).

X-ray diffraction was used to determine the phase composition of the sintered C.S. samples, crushed and ground into powder using mortar and pestle (Figure 15). A comparison of the X-ray diffraction patterns of pre- and post-sintered samples show two interesting differences. First and foremost, the rutile seen in the pre-sintered powders, Figure 10, is no longer present, suggesting the incorporation of rutile in the BGR phase(s). Second, there is a shift in the peak position, i.e. an increase in the separation between the peaks at ~27 and 29 °2θ after sintering.

The conditions present during SPS are different from those present during the pre-sintering heat treatment of the C.S. powders in several ways. First, the maximum temperature is different; ~1300 °C for SPS and 1400 °C for the powder heat treatment. If

the phase diagram presented by Kamiya et. al. in Figure 7 is accurate, then all BGR phases above n=15 (n ≥ 17) should be stable at 1300 °C. Therefore, the maximum temperature difference should not have any effect on the phase stability for samples of n-value greater than 15. Next, the atmospheric conditions are different. It is well known that graphite dies used for SPS that encapsulate the sample create a reducing environment, significantly greater than in air. The extent to which both of these differences contributed to the difference in the X-ray diffraction patterns is discussed below.

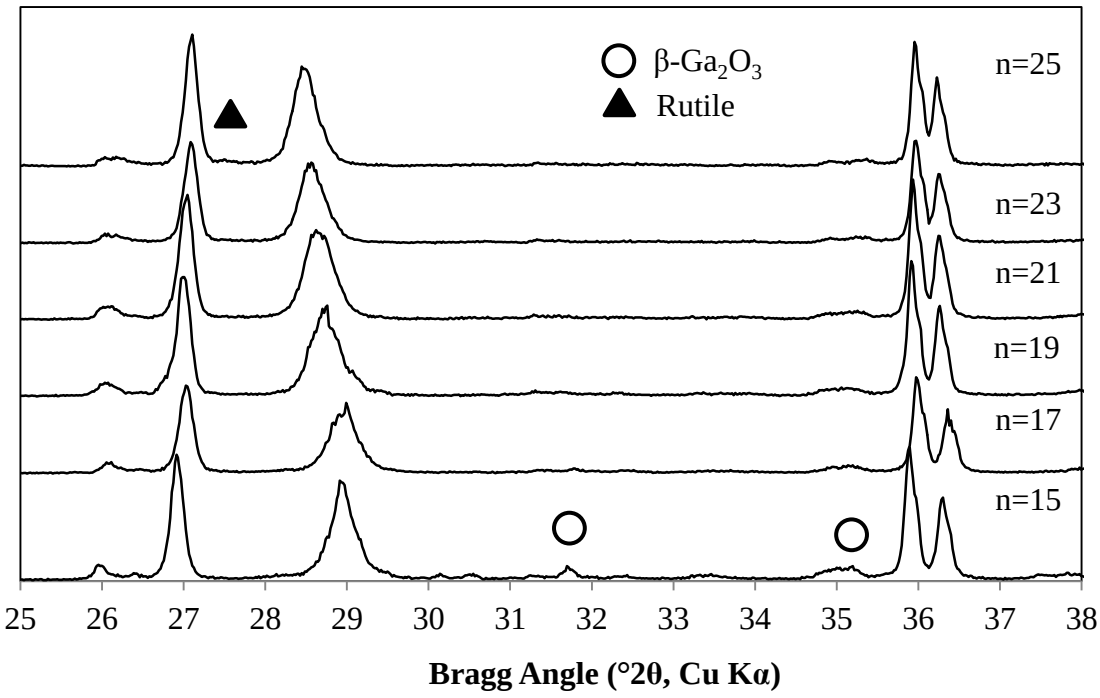


Figure 15. Powder XRD patterns of C.S. BRG samples, SPS sintered and ground.

As evidenced by the disappearance of the rutile peaks, the sintering by SPS clearly facilitated the continued reaction of rutile with the BGR phase(s) present in the pre-SPS sintered samples. It is possible that the exposure to high temperatures and/or the reducing conditions are responsible for this. Regardless of the cause, though, one would expect this reaction to result in an increase in the amount of larger n-value BGRs (higher Ti:Ga ratio), with a corresponding decrease in the lower n-value content. As discussed previously and shown in Figure 13, there is a trend of decreasing peak separation with

increasing n-value from n=15 to 25. However, this was not observed. Instead, there is a notable increase in peak separation seen in all post-sintered samples.

As stated above, it is possible that the reducing sintering conditions of SPS are responsible for, or contributed to, the incorporation of the residual rutile into the BGR phases in all samples where present. As seen in Figure 15, there is a trend between peak separation of the two diffraction peaks at roughly 27 and 29 °2θ and overall composition of the post-sintered samples; peak separation decreases with increasing n-value (decreasing gallia content). Figure 16 shows this difference in *d*-spacing between the two main peaks (peak separation) as a function of composition for the C.S. and S.S. samples, both pre- and post-sintered. The pre- and post-sintered C.S. sample all show a decrease in *d*-spacing difference (Δ*d*) with increasing n-value, however the magnitudes of the differences are slightly greater post-sintering, and is seen systematically across the compositional range. This is indicative of some amount of lattice distortion resulting from sintering. Given that spark plasma sintering creates a reducing environment, a substoichiometric, oxygen-deficient sample is expected as a result. Therefore, the observed peak separation increase, and hypothesized lattice distortion, is possibly a result of the formation of oxygen vacancies during sintering. Additionally, the change in sample color from an opaque yellow powder to a dark blue sintered pellet is evidence that SPS sintering produces significantly reduced BGR samples.

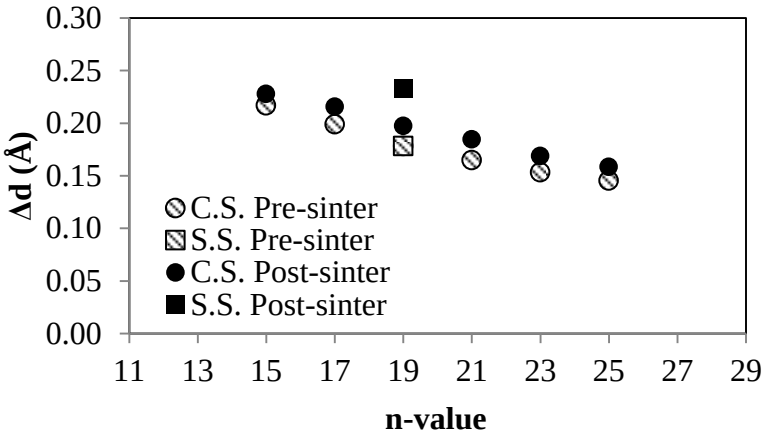


Figure 16. Δd (*d*-spacing) vs. n-value for pre- and post-sintered C.S. and S.S. samples (error bars are within data markers).

When compared to the magnitude of peak separation, and $\Delta d$, seen in the C.S. samples, however, the S.S. sample shows significantly greater increase in value post-sintering, seen in Figure 17(a-c). Unlike the near match in peak locations between the diffraction patterns of C.S. and S.S. powder samples seen in Figure 12, there is a notable difference in the peak locations post-sintering, Figure 16 and Figure 17(a). If the above hypothesis relating the increase in peak separation post-sintering in the C.S. samples to lattice distortions caused by the presence of oxygen vacancies generated by reductive sintering conditions, then the increase in separation magnitude suggests that there is greater lattice distortion in the S.S. prepared sample compared to C.S. samples. This difference in the degree of lattice distortion between the two preparation methods is attributed to nitrogen contamination during combustion synthesis. Combustion synthesis is a known method for doping $TiO_2$ samples with nitrogen, where the nitrogen occupies oxygen sites within the lattice. Therefore, it is hypothesized that the presence of nitrogen on oxygen sites during reduction inhibited some lattice distortion as the nitrogen will effectively act as non-reducible entities within the anion sublattice. This subject of nitrogen substitution on oxygen sites and its effects on BRG will be further explored in later sections.

Also evident in Figure 17(c) is that there is peak asymmetry resulting from sintering the S.S. sample, seen as an increase in bumpy peak line texture and broadening. This would seem to indicate that there is a partial breakdown in the homogeneity of the BRG phase, possibly resulting in a distribution in BGR phases close to the intended, as hypothesized above pertaining to C.S. sample peak broadness. Given that this n=19 S.S. sample was sintered at a temperature, roughly 1300 °C, near but within the n=19 phase stability region (Figure 7), a breakdown of the sample is not expected. However, it is possible that the reducing sintering conditions could have affected this phase stability region, effectively moving it to a higher temperature, greater than the sintering temperature.

Additionally, there is no presence of reduced $TiO_2$ phases, Magnèli phases, apparent in the XRD patterns of the sintered samples. Magnèli phases in $TiO_2$ are created through intense reduction and removal of oxygen from the rutile lattice, resulting in the formation of the crystallographic shear planes. As the presence of these CSPs

significantly changes the rutile lattice, the powder X-ray diffraction patterns of these phases differ greatly from that of stoichiometric rutile. Given that there are no new, missing, or substantially shifted peaks in the sintered BGR patterns compared to the pre-sintered powder, the results seem to indicate that there are no CSPs present in the reduced BGR samples.

To summarize, SPS-sintered n=15 samples, like those processed in air, contain beta-gallia in addition to a BGR phase (or phases). Also, the SPS-sintered samples prepared with n>17 have not shown to be truly "single phase" materials, but rather are likely a mixture of BGR phases with a range of n-values. Further experimentation would be required to determine the feasibility of attaining truly single phase BGR materials with large n-values using these preparation methods, but was not conducted in this work.

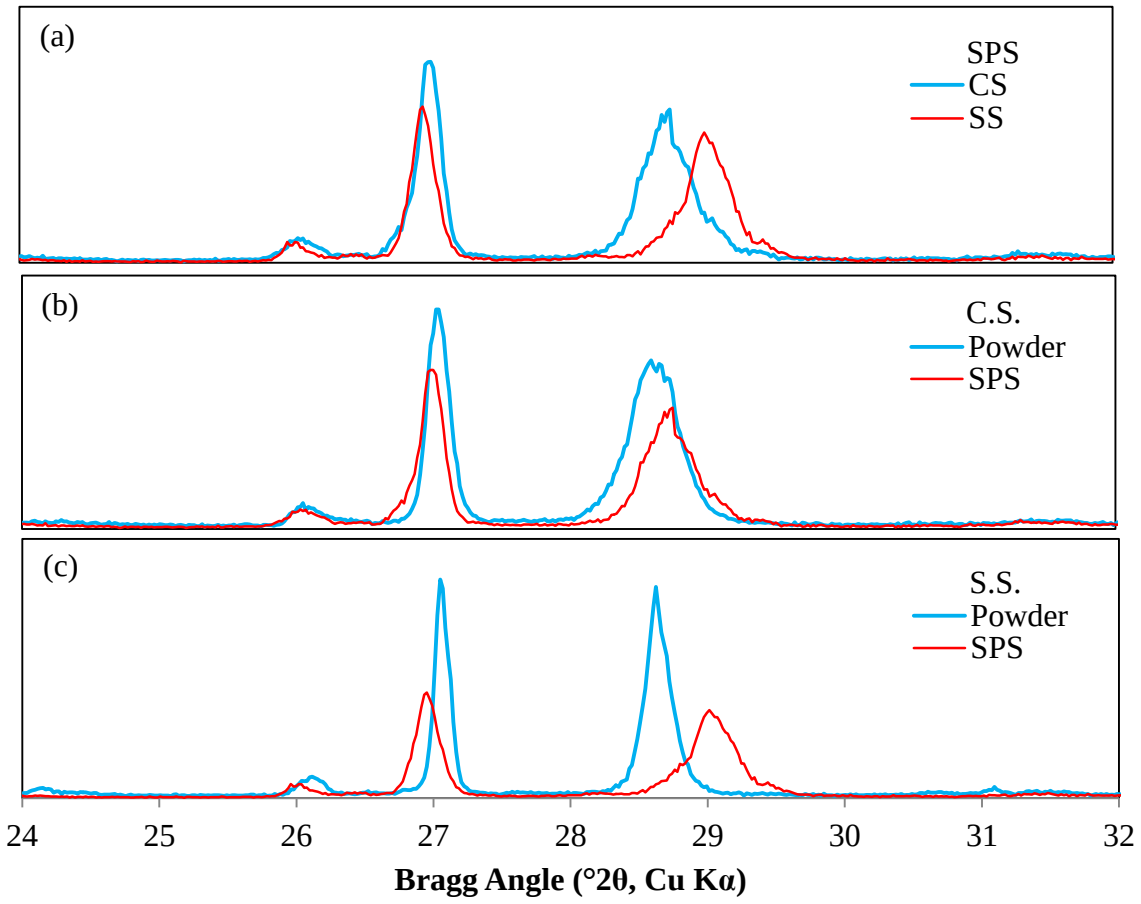


Figure 17. Powder XRD patterns of (a) C.S. and S.S. n=19 samples, SPS sintered and ground, (b) n=19 C.S. powder vs. SPS, and (c) n=19 S.S. powder vs. SPS.

## B. Electrical Properties

### 1. Electrical Conductivity and Thermopower

The measured thermopower (Seebeck coefficient) and electrical conductivity data for all samples are shown in Figure 18 and Figure 19, respectively. The negative magnitude of thermopower indicates that spark plasma sintered BRG is an n-type semiconductor. With the exception of the anomalous behavior in thermopower of the n=15 sample (possible due to the presence of unreacted gallia), all of the samples show the same relative trend with temperature; there is overall no change in thermopower from room temperature to around 400 °C. This suggests that there is no thermal generation of carriers over this temperature range. The electrical conductivity data over this same temperature range shows a nearly linear increase with increasing temperature. This in conjunction with the lack of temperature dependence of thermopower indicates that BRG exhibits thermally activated carrier mobility, meaning that below 400 °C electron transport is accomplished through the polaron hopping conduction mechanism.

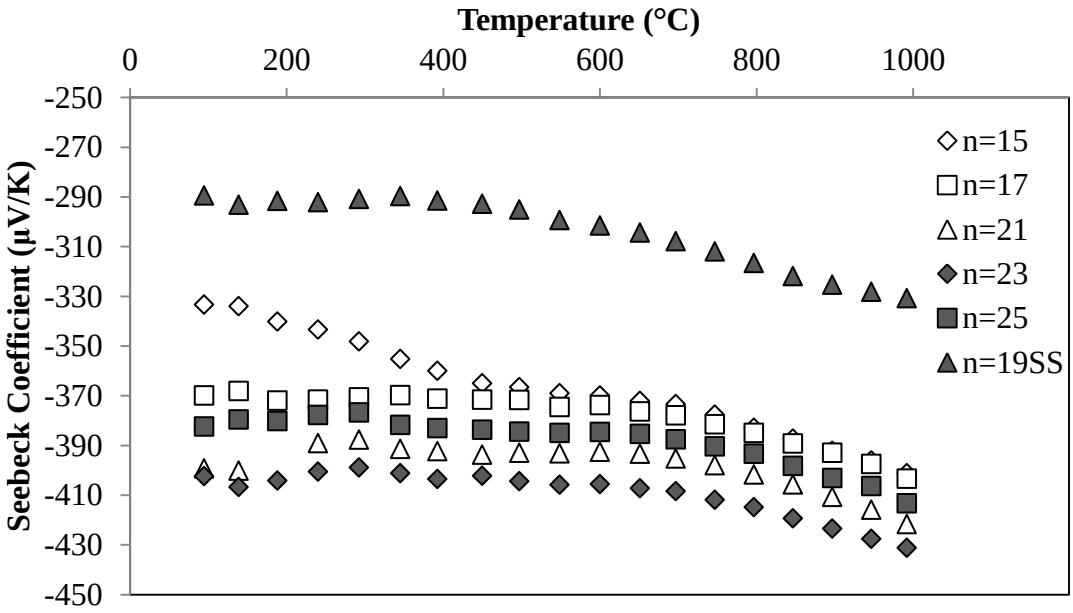


Figure 18. Thermopower (1,4) as a function of temperature for all BRG samples, C.S. and S.S.

Above 400 °C there is an increase in Seebeck coefficient in all samples with increasing temperature, while the increase in magnitude of electrical conductivity is decreasing. Both trends indicate that the amount of charge carriers decreases with increasing temperature; electrical conductivity is linearly proportional to charge carrier concentration while Seebeck coefficient is related inversely. Given the gradual nature of the change in both properties from 400 °C upwards, it is unlikely that the change in behavior is attributable to a change in conduction mechanism; one would expect a more abrupt change. Therefore it is proposed that the observed changes in properties in this high temperature region are attributable to surface oxidation and decomposition of the samples. This is supported by the presence of a white scale on the surface of the samples after a measurement cycle that was determined to be β-gallia and rutile by X-ray diffraction. Even though all samples were measure in argon, there was approximately 30 ppm of oxygen present in the flow gas which could have led to oxidation at high temperatures, and the fact that these samples show this change in surface composition even at temperatures as moderate as 500 °C indicates significant sensitivity to oxidation and decomposition. This oxidation and decomposition, however, did not appear to affect the bulk of the samples; the measured conductivity and thermopower were repeatable when the surface layers were removed through grinding.

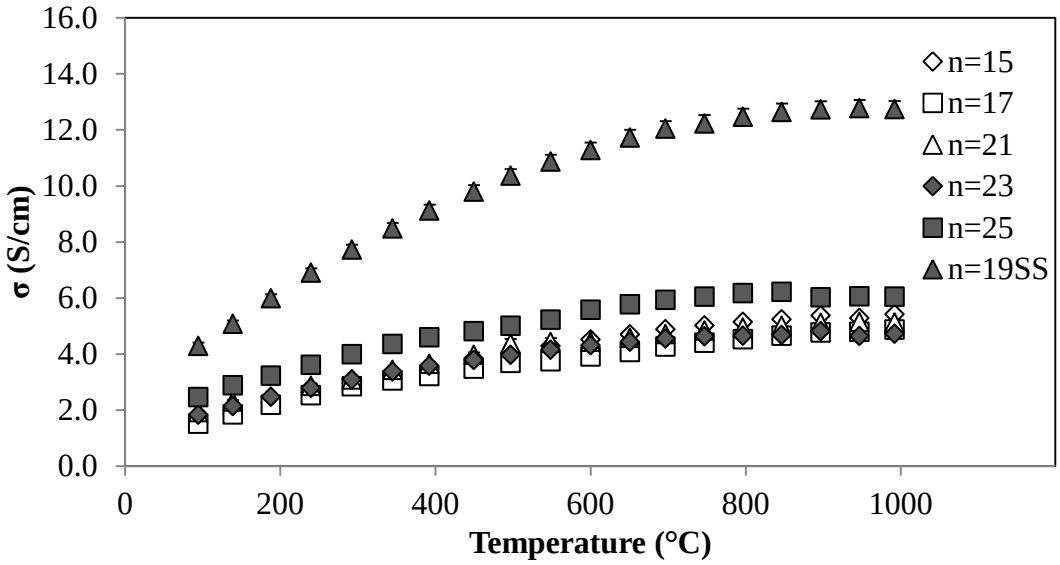


Figure 19. Electrical Conductivity as a function of temperature for all BRG samples, C.S. and S.S.

As seen in Figure 18, thermopower increases in magnitude with n-value from 15 to 23, upon which the next compositional step to n=25 shows a significant decrease in magnitude (similar to n=15). Comparing this to the electrical conductivity results, there is no discernable trend as a function of composition with the exception of the n=25 sample showing the highest measured values. This corresponds with the low Seebeck coefficient, indicating that the n=25 samples may possess a higher intrinsic carrier concentration relative to all other compositions tested. The hypothesis at the onset of this work regarding electrical properties was that the $TiO_2$ layers would be the primary pathways for electrical conduction, therefore carrier concentration was expected to increase with n-value and thermopower to decrease. With the exception of the n=25 sample, the results do not support this hypothesis. However, it is suspected that observed differences between thermopower and electrical conductivity with respect to composition are likely the result of different concentrations of nitrogen impurities (discussed below) between compositions, as well as differences in processing conditions such as reaction temperature (adiabatic flame temperature) and grain boundary conditions.

At first glance the differences between the S.S. and C.S. samples are plainly evident; the S.S. sample shows a significant lower thermopower magnitude with a higher magnitude of electrical conductivity. These findings suggest that there is a difference in carrier concentration resulting from the two synthesis methods, specifically that the sample prepared using solid-state synthesis possesses a greater intrinsic carrier concentration compared to those synthesized using the combustion method. This is supported by the Jonker analysis of the data from the n=17 C.S., n=21 C.S., and n=19 S.S. samples at 300, 400, and 500 °C, seen in Figure 20. The n=17 and 21 C.S. samples were chosen because there is no data from an n=19 C.S. sample, and therefore the Seebeck coefficients of this sample is assumed to be intermediate between the two. As seen in Figure 20, the slopes of the linear trendlines for the samples at 300, 400 and 500 °C are 90.7, 88.9, and 86.7 μV/K, respectively. In the extrinsic non-degenerate region of a Jonker plot, the slope of the line will have a slope of 86.15 μV/K ($k_B/e$)[43]. Therefore, differences in thermopower and electrical conductivity of samples that fall along this line are attributed to differences in extrinsic carrier concentration. Since the slopes of the lines from the present Jonker analysis are arguably equal to 86 μV/K (given measurement error

and variation), the differences between the electrical properties of the n=19 S.S. sample and the C.S. samples (n=19 C.S., mainly) are concluded to be due to differences in extrinsic carrier concentration.

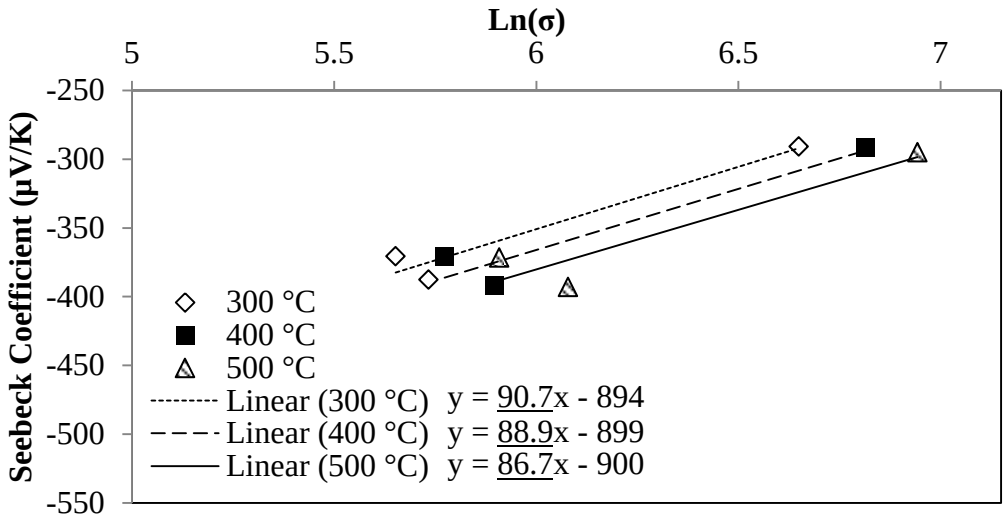


Figure 20. Jonker plots of n=17 C.S., n=21 C.S., and n=19 S.S. at 300, 400 and 500 °C.

As mentioned previously, combustion synthesis is a known method for preparing samples doped with nitrogen[44,45], including titanium dioxide[46-49], as some of the precursors involved in the reaction are nitrates or nitrogen compounds. Therefore it is hypothesized here that the differences in electrical properties of the S.S. and C.S. samples are a result of nitrogen impurities in the C.S. samples, occupying oxygen sites within the lattice and acting as an acceptor-type dopant. The literature on this subject states that when nitrogen is introduced into the $TiO_2$ rutile lattice that it takes an electron from a local $Ti^{3+}$ atom, allowing it to occupy an oxygen lattice site as a $N^{3-}$. A local charge imbalance results from the now $N^{3-}$ sitting on an $O^{2-}$ site, which in $TiO_2$ is compensated through the formation of oxygen vacancies ($V_O$)[50-53], seen in equation 12 below.

$$2Ti_{Ti}^{x} + 4O_{O}^{x} + N_2 \rightarrow 2Ti_{Ti}^{x} + O_{O}^{x} + 2N_{O}' + V_{O}^{\cdot\cdot} + \frac{3}{2}O_2 \qquad (12)$$

While this equation represents the defect formation in pure $TiO_2$ (rutile), it is possible that this relation can also represent defect formation in BGR since its structure consists primarily of large slabs of $TiO_2$. However, the formation of oxygen vacancies as the primary compensating defect is not the only possible explanation for the differences in measured thermopower and electrical conductivity, assuming those differences stem from differing carrier concentrations. In response to the charge imbalance caused by the nitrogen, electron holes could also be generated as compensating defects instead of oxygen vacancies (Equation 13), leading to a lower electron concentration in combustion synthesized n-type BRG samples.

$$2Ti_{Ti}^{x} + 4O_{o}^{x} + N_2 \rightarrow 2Ti_{Ti}^{x} + 2O_{O}^{x} + 2N_{O}' + 2h^{\cdot} + O_2 \tag{13}$$

As stated previously, it is presently hypothesized that BGR conducts electronically through the polaron hopping mechanism, meaning that conduction through the crystal occurs by the "hopping" of electrons from $Ti^{3+}$ sites to local $Ti^{4+}$ sites. When assumed that these generated holes from equation 13 associate themselves with $Ti^{3+}$ sites, $Ti^{4+}$ sites result, this leads to a reduction in total possible hopping sites and overall a reduction in conductivity. Equation 14 is an expression that relates the Seebeck coefficient with the ratio of $Ti^{4+}/Ti^{3+}$ in $TiO_2$[54]:

$$\alpha = -\frac{k_B}{e}\ln\left(\frac{g_3}{g_4}\frac{x}{1-x}\right) \tag{14}$$

where α is the Seebeck coefficient, $k_B$ is the Boltzmann constant, e is the elementary charge, $g_3$ and $g_4$ are the total number of orbital spin configurations of $Ti^{3+}$ and $Ti^{4+}$, respectively, and x is the fraction of $Ti^{4+}$ sites. $g_3$ is calculated to be six (6), as $Ti^{3+}$ has a 3d-electron in three $t_{2g}$ orbitals; the product of 3 (orbitals) and (2S+1), where S=1/2, is six. Since $Ti^{4+}$ has no 3d-electron, $g_4$ is calculated to be 1[54]. Table 2 shows the theoretical fractional $Ti^{4+}$ and $Ti^{3+}$ composition of C.S. and S.S. prepared samples. The "n=19 C.S. (theo.)" sample Seebeck value is theoretical and based on the linear trend seen in the

thermopower measurements as a function of compositions seen in the C.S. samples, resulting in a value between that of n=17 and 21.

Table 2. Calculated Fractional Composition of $Ti^{4+}$ and $Ti^{3+}$ in C.S. and S.S. Samples at 400 °C.

| Sample | α (μV/K) | $Ti^{4+}$ | $Ti^{3+}$ |
|---|---|---|---|
| **n=17 C.S.** | -371 | 0.925 | 0.075 |
| **n=21 C.S.** | -392 | 0.940 | 0.060 |
| **n=19 C.S. (theo.)** | -381 | 0.933 | 0.067 |
| **n=19 S.S** | -291 | 0.830 | 0.170 |
| **n=25 C.S.** | -383 | 0.935 | 0.065 |

When compared with the n=19 S.S. sample, the calculated $Ti^{3+}$ composition of the n=19 C.S. value is roughly 10.3 mol% lower (6.7% vs. 17.0%). If the theoretical composition of n=19 is $Ga_4Ti_{15}O_{36}$, then overall there is approximately 27.3 mol% Ti, 7.2 mol% Ga, and 65.5% O per unit cell. As seen in Equation 12, the presence of nitrogen in the rutile lattice can result in the transfer of an electron from a $Ti^{3+}$ to stabilize the $N^{3-}$ and the formation of an oxygen vacancy. Using the following assumptions, the difference between the $Ti^{3+}$ and $Ti^{4+}$ contents of n=19 C.S. and S.S. can be correlated to the level of nitrogen contamination in the C.S. sample: (1) oxygen vacancies are the compensating defects for nitrogen substitution into the anion sublattice, (2) that there is one hole generated for each substituted nitrogen, (3) that the holes associate themselves with local $Ti^{3+}$ ions forming $Ti^{4+}$, and that (4) the S.S. sample is free of nitrogen contamination. This value was calculated to be roughly 2.81 mol% nitrogen in the entire system (10.3% of 27.3 mol% Ti), which equates to 1.58 atoms of nitrogen per formula unit ($Ga_4Ti_{15}(O_{34.42},N_{1.58})$), or 4.40 mol% N on O sites (1.58 N ÷ 36 O sites).

The second possible mechanism for charge compensation, seen in Equation 13, involves the formation of holes instead of oxygen vacancies. Therefore, assuming that (1) holes are the compensating defects for nitrogen substitution into the anion sublattice, (2) that there are two hole generated for each substituted nitrogen (one hole from the $N^{3-}$ stabilization and one as a charge compensating defect), and (3) and (4) stated above, 0.79 atoms of nitrogen per formula unit ($Ga_4Ti_{15}(O_{35.21},N_{0.79})$), or 2.20 mol% N on O, was

calculated to be the nitrogen content in the n=19 C.S. sample. While the typical method for producing nitrogen doped rutile samples, heat treatment of $TiO_2$ in an gaseous ammonia atmosphere, has shown to achieve at most 2 at.% doping, Lynch et. al.[55] reported the synthesis of highly branched rutile nanostructures with between 2 and 17 at % nitrogen doping, both substitutional and interstitial, using a solution chemistry-based approach. Additionally, they found that the samples with higher overall nitrogen content tended to possess a larger percentage of substitutional nitrogen. Therefore, the above calculated 4.40 and 2.20 mol % substitutional nitrogen doping in the n=19 BGR sample is not an unreasonable assertion.

### 2. Activation Energy and Hopping Mobility

As stated previously, the change in electrical properties with temperature above 400 °C is attributed to oxidation. The region below 400 °C, however, shows behavior indicative of electronic conduction through the polaron hopping mechanism. The absence of a temperature dependence in thermopower means that there is no thermal generation of carriers. This leads to the conclusion that the activation energy associated with electronic conduction as measured through D.C. conductivity is entirely representative of the activation energy of carrier mobility. An Arrhenius plot was used to determine activation energy values for all samples, an example of which is shown in Figure 21. Given that these samples have displayed polaron type conduction, electrical conductivity was plotted as $\ln(\sigma T)$ vs. $1/T$.

The respective activation energy values were determined, in eV, through the normalization of the linear slope values, seen in Figure 21, with the Boltzmann constant, and are listed in Table 3. Excluding the anomalous low-temperature data from the n=15 thermopower sample and scattering in the n=21 sample data (both treated as outliers), all of the samples, both C.S. and S.S., show carrier generation activation energies ($E_\alpha$) very close to zero, indicating independence with temperature. Additionally, the data shows that there is no change in the activation energies for mobility ($E_\mu$), which when $E_\alpha \approx 0$ effectively equals $E_\sigma$, with changes in composition. All samples show an activation energy for polaron mobility of around 0.052 eV, which is the same order of magnitude that was observed for rutile (0.098eV)[41].

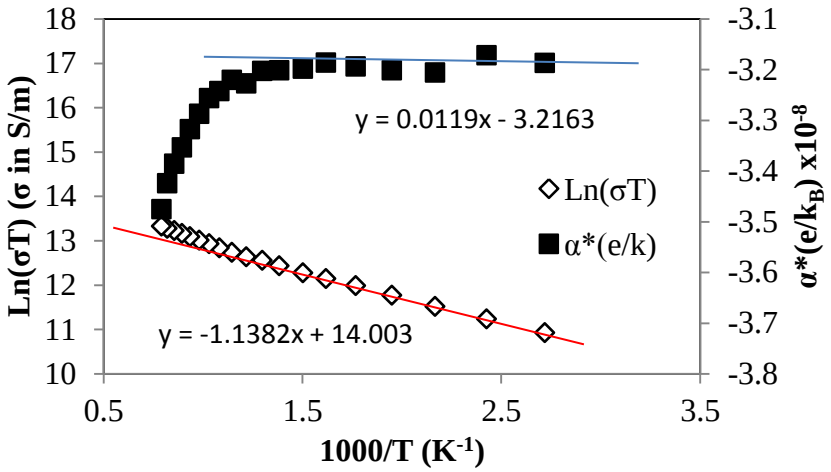


Figure 21. Combined analysis plot for carrier activation energy determination, $\ln(\sigma T)$ and $\alpha \cdot (e/k_B)$ vs. 1000/T (n=17).

Table 3. Activation Energies (eV) of Conduction for BGR S.S. and C.S. Samples, where $E_\sigma$ is the Energy for Conduction Overall, $E_\alpha$ is the Carrier Generation Activation Energy, and $E_\mu$ is the Mobility Activation Energy ($E_\sigma$-$E_\alpha$), Over a Temperature Range of 100-500 °C.

| **n-value** | **15** | **17** | **21** | **23** | **25** | **19 S.S.** |
|---|---|---|---|---|---|---|
| $\mathbf{E_\sigma}$ | 0.056 | 0.055 | 0.054 | 0.053 | 0.052 | 0.053 |
| $\mathbf{E_\alpha}$ | 0.033 | 0.001 | 0.056 | 0.000 | 0.002 | 0.002 |
| $\mathbf{E_\mu}$ | 0.023 | 0.053 | -0.002 | 0.053 | 0.050 | 0.052 |

The electron hopping mobility for n=25 was determined using calculated carrier concentration values along with equation 1 ($\sigma = e \cdot n \cdot \mu$). The estimated carrier concentration was calculated using the following equation:

$$n = \frac{a \cdot c \cdot x_{Ti}}{V_{UC}} \tag{15}$$

where a is the number of formula units per unit cell, c is the number of titanium atoms per unit cell, $x_{Ti}$ is the fraction of $Ti^{3+}$ atoms (Table 2), and $V_{UC}$ is the volume of the unit cell. The crystal structure data used to calculate the unit cell volume (1541.76 $Å^3$) was taken from work done by Lloyd et. al.[31]: a = 51.80 Å, b = 2.975 Å, c = 10.302 Å, and β =

103.80°. A carrier mobility of 0.1 $cm^2/V \cdot s$ is generally viewed as the distinction between polaron and band conduction mechanisms, with polaron conduction mobility values below this threshold[56]. As seen in Figure 22, all of the mobility values calculated for n=25 fall well below this threshold, with a mobility of 0.017 $cm^2/V \cdot s$ at 400 °C, further supporting conduction by polar hopping.

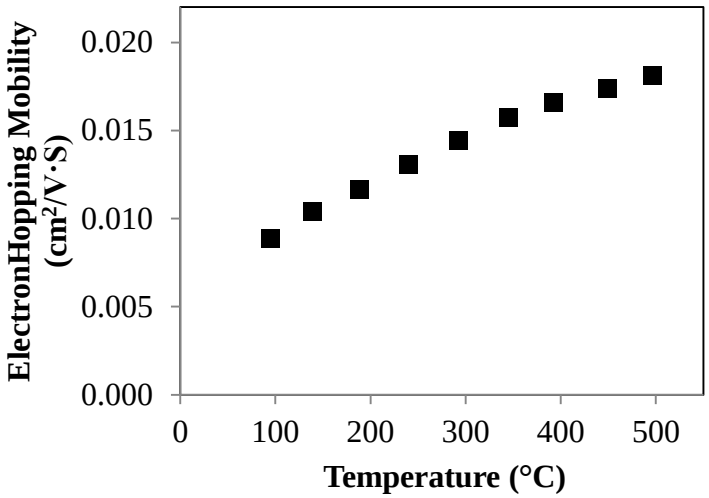


Figure 22. Calculated electron hopping mobility for n=25 C.S. sample as a function of temperature.

## C. Thermal Properties

### 1. Thermal Diffusivity

The thermal diffusivity data, measured using the laser flash method, are shown below in Figure 23. All samples show a decrease in diffusivity with increasing temperature; an expected result due to the increase in phonon-phonon scattering. Additionally, there is a lack of any discernable trend in diffusivity as a function of composition (C.S. samples) due to the scattering in the data and the error of measurement method overall. Another factor which could contribute to the similarity in measured diffusivity results is the possibility of a heterogeneous phase composition; the distribution of phases close to the intended composition, hypothesized in a previous section. The individual BGR phases within the distribution could be contributing such that the overall

measured thermal diffusivity is effectively as an arithmetic average of individual phase diffusivities. This notion, however, assumes that there would in fact be a change in diffusivity with composition. Reflecting back on the XRD patterns shown in Figure 15, there is notable overlapping between the peaks areas of the sample compositions tested, which indicates the similarities in sample phase compositions overall. The thermal diffusivity data of the n=19 S.S. sample is also notably lower than those of the C.S. prepared samples. This is attributed to the higher degree of porosity in the S.S. sample, confirmed through both Archimedes density measurement (Table 1) and scanning electron microscopy (Figure 14c).

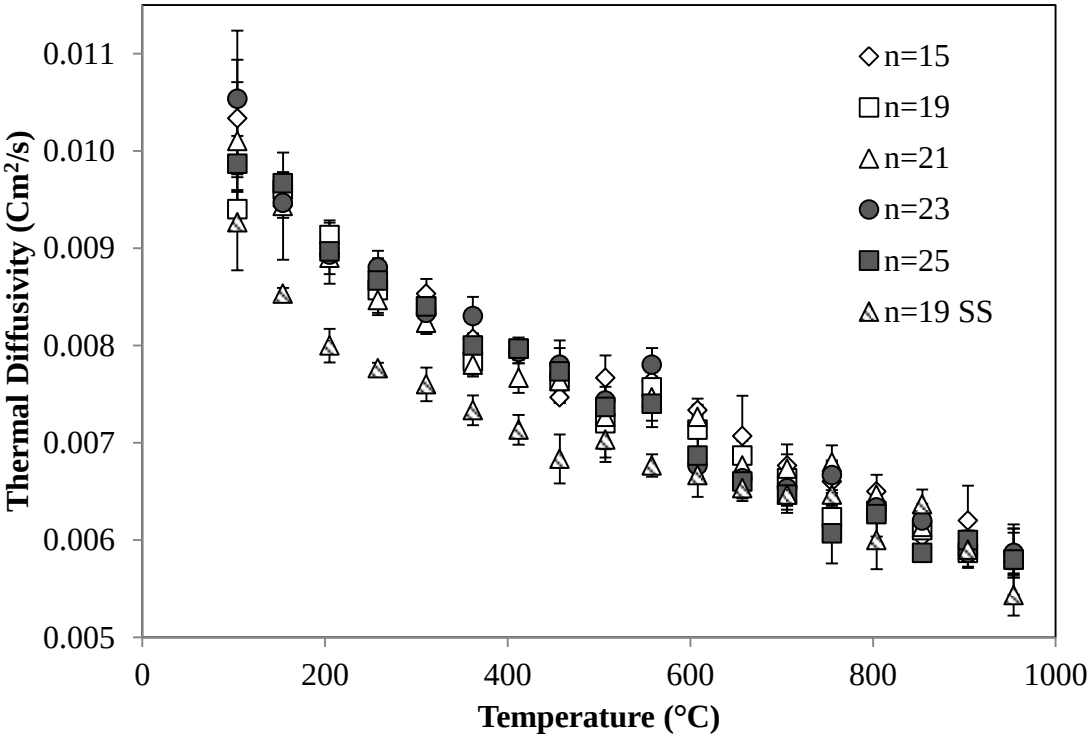


Figure 23. Thermal diffusivity as a function of temperature for all BGR samples, C.S. and S.S.

### 2. Calculated Heat Capacity and Thernal Conductivity

The specific heat capacities of the samples as a function of temperature were determined simultaneously with thermal diffusivity using the laser flash method with an

aluminum oxide standard reference material. However, there is considerable scattering in the data, and an example of this is shown in Figure 24. Therefore, for the calculation of thermal conductivity, and therefore ZT, for these materials, the heat capacity data used was smoothed using a second order polynomial, as seen in Figure 24. Due to the significant level of scatter in the data, no trend between composition and specific heat capacity of the BGR samples could be concluded.

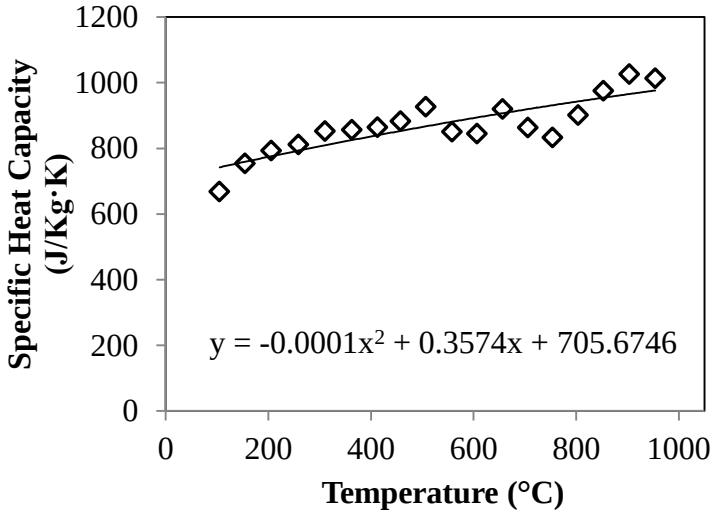


Figure 24. Measured specific heat capacity of n=21 C.S. with a third order polynomial trendline.

The calculated thermal conductivity values of n=19 S.S. and n=21 C.S. are shown in Figure 25, along with the data collected by Harada et. al.[8] for hot-pressed, polycrystalline samples of $TiO_2$ and $TiO_{1.90}$. XRD phase analysis of the $TiO_{1.90}$ sample was matched to the indexed $Ti_6O_{11}$ Magnèli phase. The lower magnitude of thermal conductivity of the n=19 S.S. sample compared with the n=21 C.S. sample (roughly 25% lower) is attributed to the lower thermal diffusivity discussed in the above section along with the lower bulk density, due to the presence of pores in the microstructure. However, when compared with stoichiometric $TiO_2$, both samples show significantly lower values; roughly 36% (n=21) and 45% (n=19) lower at 100 °C, and 28% (n=21) and 37% (n=19) lower at 400 °C. Additionally, the thermal conductivities of both samples at low temperatures are similar to those of the $Ti_6O_{11}$ Magnèli phase sample. To reiterate, the

present hypothesis of this work that these BGR materials will behave like rutile $TiO_2$ with layers of β-gallia separating the sections of rutile, by which the rutile is the dominant pathway of electrical and thermal conduction while the gallia layers act as phonon scattering interfaces. If this hypothesis is correct, then the similarity between the measured thermal conductivity of the BGR samples and the $Ti_6O_{11}$ sample, all vastly lower than that of stoichiometric $TiO_2$, suggests that the presence of the gallia was a significant contributing factor to the reduced values.

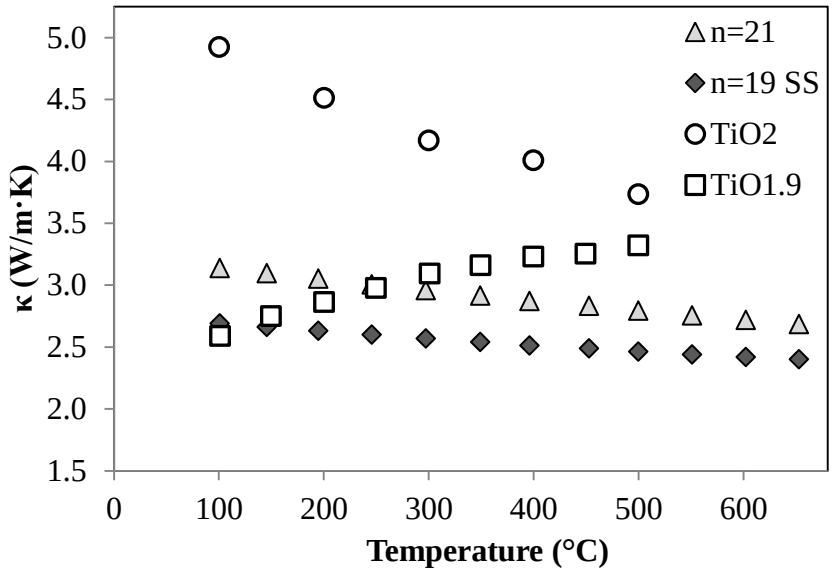


Figure 25. Thermal conductivity of n=21 C.S. and n=19 S.S. compared to polycrystalline $TiO_2$ and $TiO_{1.90}$[8].

## D. Generalized Thermoelectric Properties

As seen in Figure 26, amongst the samples prepared through combustion synthesis there is a general trend of increasing power factor ($\sigma \cdot \alpha^2$) with increasing n-value. This is attributed to the trend seen in thermopower; increasing value with increasing n-value from 15 to 23. Although the n=25 sample showed a lower thermopower values over the temperature range, the fact that this composition showed the highest electrical conductivity overall led to it displaying the highest power factor among the C.S. samples. Compared to all of the samples tested, the n=19 S.S. sample

showed the highest power factor, attributed to the significantly greater magnitude of electrical conductivity.

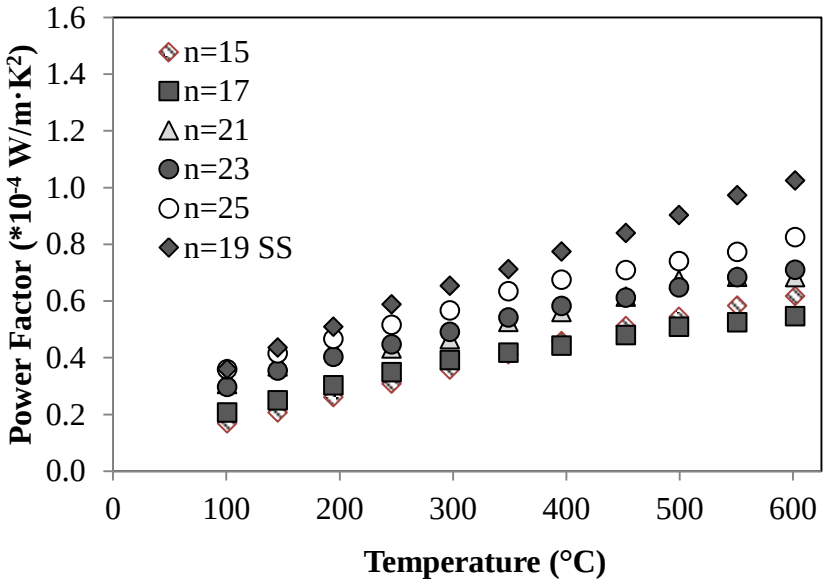


Figure 26. Power factor of all samples measured, both C.S. and S.S.

The power factor values, seen in Figure 27a, of the samples studied in this work are significantly lower than those of the $Ti_6O_{11}$ ($TiO_{1.90}$) sample from the literature, which is attributed to the two order of magnitude difference in electrical conductivity with thermopower values ranging from 130 to 150 μV/K from room temperature to 500 °C. Consequently, given that the measured thermal conductivity values for the BGR samples are similar to those of the Magnèli phase sample in conjunction with the high power factor, the resulting ZT values of the BGR samples fall greatly below that of the $Ti_6O_{11}$ sample; the $Ti_6O_{11}$ sample ZT is roughly five times greater than those for BGR at 400 °C. A plot of these ZT values is shown in Figure 27b. However, when comparing the n=19 S.S. sample to the n=21 C.S. sample, there is still a significant difference; the n=19 sample ZT is 57% greater than that of the n=21 C.S at 400 °C. This is attributed to both the higher power factor and the lower thermal conductivity of the n=19 S.S. sample. Overall, though, the ZT of the best performing n=19 S.S. sample at 400 °C is only 0.02, which is more than an order of magnitude lower than needed for use in a commercial TEG device (ZT~1).

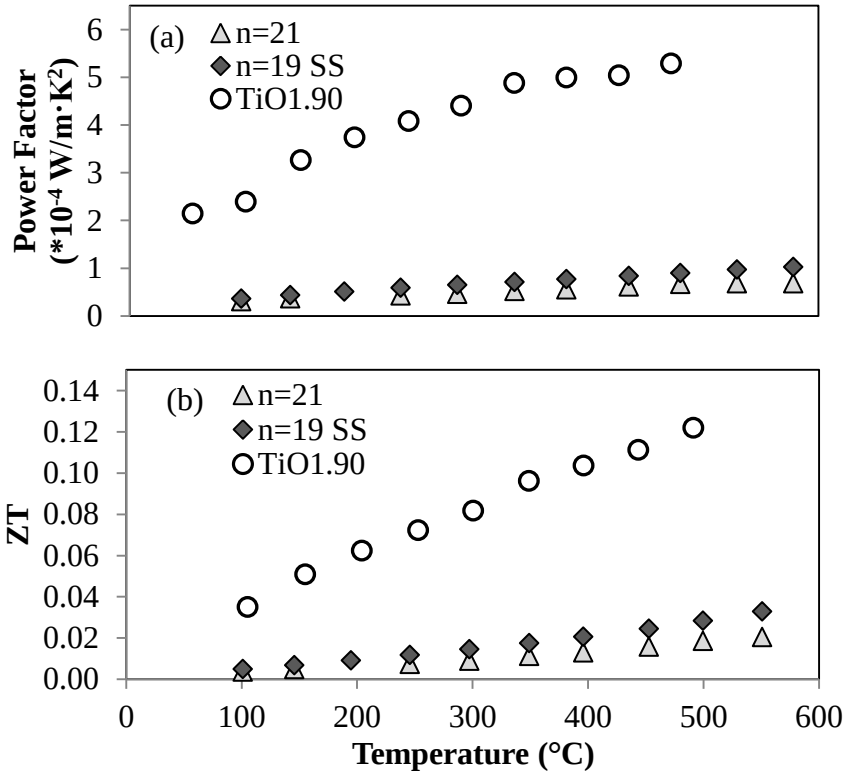


Figure 27. Power factor (a) and figure of merit ZT (b) of n=21 C.S. and n=19 S.S. compared to polycrystalline $TiO_{1.90}$[8].

# IV. SUMMARY AND CONCLUSIONS

Beta-gallia rutile intergrowth materials (BGRs) were studied as thermoelectric material candidates given their structural similarities to both reduced $TiO_2$ Magnèli phases and layered structures, such as the strontium titanate Ruddlesden-Popper series and the calcium cobaltites, with the main objective of reducing lattice thermal conductivity. Samples were prepared using both solution combustion synthesis (C.S.) and solid-state synthesis (S.S.); n=15-25 (n=odd) through combustion and n=19 with solid-state synthesis. In the as-synthesized state, the BGR powder samples show a relatively linear trend between n-value and the peak separation between the X-ray diffraction peaks at approximately 27 and 29 °2θ. Additionally, the C.S.-prepared samples show significantly greater peak broadening and asymmetry compared to the n=19 S.S. sample, possibly due to the presence of a distribution of BGR phases close to the intended composition. This could be a result of insufficient time during the BGR phase formation heat treatment to reach homogeneity. There is also a minor rutile phase present in all samples except n=19 and β-gallia within the n=15 sample, indicating incomplete BGR phase formation.

Spark plasma sintering (SPS) was used to sinter all of the samples investigated in this study. Archimedes density measurement of the samples indicated that all of the C.S. samples were sintered to near full density (less than 0.15% apparent porosity), while the n=19 S.S. sample was sintered to almost full density (~3% apparent porosity). Powder XRD of the sintered samples revealed the disappearance of the rutile phase in all samples where present, but the β-gallia still remained in the n=15 sample. This indicates that the BGR phase is not stable below n=17 under these processing conditions. The sintering of the samples also results in a systematic shifting of diffraction peaks, attributed to a distortion in the crystal lattice from the reducing nature of SPS.

Thermopower measurements indicate that these BGR materials are n-type semiconductors. There is no observed temperature dependence of thermopower below 400 °C, indicating that there is no generation of carriers from thermal energy within this temperature range. Combined with the measured increase in electrical conductivity, it is concluded that below 400 °C these materials are polaron conductors, with all samples

showing the activation energy for carrier mobility to be on average 0.052 eV, compared to 0.098 eV for rutile $TiO_2$. Overall, there was no trend observed between electrical conductivity and n-value. All samples showed similar measured electrical conductivity values over the temperature range, except for n=25 which showed the highest electrical conductivity. Thermopower appears to increase in magnitude with increasing n-value from 15 to 23, with the thermopower of n=25 dropping to values similar to n=15. The lack of a clear trend between the electronic properties and composition is likely due to differences in processing conditions (reaction temperature) and nitrogen impurity concentration. Above 400 °C, the changes in electrical conductivity and thermopower are concluded to be related to the surface oxidation and decomposition of the BGR phase into β-$Ga_2O_3$ and rutile $TiO_2$.

The measured thermopower and electrical conductivity of the n=19 S.S. sample show values differing substantially from the C.S.-prepared samples; higher σ and lower α for n=19 S.S. It is thought to be rooted in a lower concentration of carriers present in the C.S. prepared samples resulting from acceptor-type nitrogen impurities (substituted on O sites) from the combustion synthesis process itself. It was calculated that there is 4.40 mol % (one hole per N) or 2.20 mol % (two holes per N) N on O sites that contribute to this difference in carrier concentration. These nitrogen impurities could also be responsible for the different amounts of lattice distortions observed in the XRD patterns of the sintered samples, with the n=19 S.S. sample experiencing greater distortion from the lack of nitrogen present.

Overall, there was no notable trend between thermal diffusivity and n-value, due to both the scatter in the measured data from the laser flash method and the possibility of a distribution of BGR phases present in the samples. However, the magnitude of the measured thermal conductivity for all BGR samples is on par with that of a reduced $TiO_2$ Magnèli phase, $Ti_6O_{11}$. This suggests that the presence of the β-gallia layers within the BGR structure may have been responsible for the reduction in conductivity compared to stoichiometric $TiO_2$, as hypothesized.

In general, there is an increase in power factor ($\sigma \cdot \alpha^2$) with increasing n-value among the C.S. sample, following the general trend between composition and thermopower. As such, of the samples tested in this work the n=19 S.S. sample shows the

highest measured power factor. With the lower measured thermal conductivity, this sample shows a 57% greater ZT value compared with the n=21 C.S. sample. Unfortunately, even this sample which performs best among the all BGR samples shows a ZT of only 0.02 at 400 °C, substantially lower than is required to be used in a TEG device. This is also significantly lower than the measured ZT of the $Ti_6O_{11}$ Magnèli phase sample, 0.10 at 400 °C.

# V. FUTURE WORK

The main objective of this work was to determine the impact that the presence of the β-gallia intergrowths has on thermoelectric properties, specifically thermal conductivity. Given the scatter in the laser flash data, the results were inconclusive. It is hypothesized in this work that this may be due to the presence of multiple BGR phases that are similar in composition to the intended, and are distributed throughout the samples. Therefore, the future objective for this work would revolve around producing samples with single phase character, or as close to single phase as possible. Heat treatment experiments held for greater durations and higher temperatures could indicate whether samples with homogeneous phase compositions can be produced. If this proves fruitful, then sintering experiments would be conducted to examine whether that phase uniformity can be maintained during densification in SPS. With phase pure sintered samples, greater confidence could be given to the measured thermoelectric properties as being representative solely of a single BGR phase.

Additionally, this work has raised the question of possible nitrogen contamination in the BGR samples resulting from combustion synthesis. To confirm the presence of this nitrogen, whether located in substitutional or interstitial positions, X-ray photoelectron spectroscopy (XPS) experiments could be conducted. XPS could also be used to obtain experimental estimates of $Ti^{3+}$ to $Ti^{4+}$ ratios within each sample. If nitrogen is confirmed to be present in the combustion synthesized samples, it may also be worthwhile to explore whether this nitrogen contamination could be controlled using the elemental stoichiometric coefficient.

# VI. REFERENCES


1. D. D. Pollock, *Thermoelectricity: Theory, Thermometry, Tool*. ASTM, 1985.

2. T. M. Tritt, H. Böttner, and L. Chen, "Thermoelectrics: Direct Solar Thermal Energy Conversion," *MRS Bull.,* **33** [04] 366-8 (2008).

3. T. M. Tritt and M. Subramanian, "Thermoelectric Materials, Phenomena, and Applications: A Bird's Eye View," *MRS Bull.,* **31** [03] 188-98 (2006).

4. J. Yang and T. Caillat, "Thermoelectric Materials for Space and Automotive Power Generation," *MRS Bull.,* **31** [03] 224-9 (2006).

5. G. J. Snyder and E. S. Toberer, "Complex Thermoelectric Materials," *Nat. Mater.,* **7** [2] 105-14 (2008).

6. P. Chaikin, "An Introduction to Thermopower for Those Who Might Want to Use It to Study Organic Conductors and Superconductors"; pp. 101-15 in *Organic Superconductivity.* Springer, 1990.

7. S. L. Shinde and J. Goela, *High Thermal Conductivity Materials*. Springer New York, 2006.

8. S. Harada, K. Tanaka, and H. Inui, "Thermoelectric Properties and Crystallographic Shear Structures in Titanium Oxides of the Magneli Phases," *J. Appl. Phys.,* **108** [8] 083703 (2010).

9. K. Koumoto, I. Terasaki, and R. Funahashi, "Complex Oxide Materials for Potential Thermoelectric Applications," *MRS Bull.,* **31** [03] 206-10 (2006).

10. G. A. Slack, *Crc Handbook of Thermoelectrics*. CRC Press, 407, 1995.

11. K. Koumoto, Y. Wang, R. Zhang, A. Kosuga, and R. Funahashi, "Oxide Thermoelectric Materials: A Nanostructuring Approach," *Annu. Rev. Mater. Res.,* **40** 363-94 (2010).

12. W. Wunderlich, S. Ohta, H. Ohta, and K. Koumoto, "Effective Mass and Thermoelectric Properties of $SrTiO_3$-Based Natural Superlattices Evaluated by Ab-Initio Calculations," ICT 2005. 24$^{th}$ International Conference on Thermoelectrics, 252-5 (2005).

13. S. Ohta, T. Nomura, H. Ohta, M. Hirano, H. Hosono, and K. Koumoto, "Large Thermoelectric Performance of Heavily Nb-Doped $SrTiO_3$ Epitaxial Film at High Temperature," *Appl. Phys.Lett.,* **87** [9] 092108 (2005).

14. S. Ohta, H. Ohta, and K. Koumoto, "Grain Size Dependence of Thermoelectric Performance of Nb-Doped $SrTiO_3$ Polycrystals," *J. Ceram. Soc. Jpn.,* **114** [1325] 102-5 (2006).

15. S. Ruddlesden and P. Popper, "The Compound $Sr_3Ti_2O_7$ and Its Structure," *Acta Crystallogr.,* **11** [1] 54-5 (1958).

16. K. H. Lee, S. W. Kim, H. Ohta, and K. Koumoto, "Ruddlesden-Popper Phases as Thermoelectric Oxides: Nb-Doped $SrO(SrTiO_3)$ N (N= 1, 2)," *J. Appl. Phys.,* **100** [6] 063717 (2006).

17. Y. Wang, K. H. Lee, H. Ohta, and K. Koumoto, "Thermoelectric Properties of Electron Doped $SrO(SrTiO_3)_N$ (N= 1, 2) Ceramics," *J. Appl. Phys.,* **105** [10] 103701 (2009).

18. J. Haeni, C. Theis, D. Schlom, W. Tian, X. Pan, H. Chang, I. Takeuchi, and X.-D. Xiang, "Epitaxial Growth of the First Five Members of the $Sr_{n+1}Ti_nO_{3n+1}$ Ruddlesden–Popper Homologous Series," *Appl. Phys. Lett.,* **78** [21] 3292-4 (2001).

19. I. Terasaki, Y. Sasago, and K. Uchinokura, "Large Thermoelectric Power in $NaCo_2O_4$ Single Crystals," *Phys. Rev. B,* **56** [20] R12685 (1997).

20. Y. Miyazaki, "Crystal Structure and Thermoelectric Properties of the Misfit-Layered Cobalt Oxides," *Solid State Ionics,* **172** [1] 463-7 (2004).

21. J. Diez, M. Torres, S. Rasekh, G. Constantinescu, M. Madre, and A. Sotelo, "Enhancement of $Ca_3Co_4O_9$ Thermoelectric Properties by Cr for Co Substitution," *Ceram. Int.,* **39** [6] 6051-6 (2013).

22. M. Torres, S. Rasekh, P. Bosque, G. Constantinescu, M. Madre, J. Diez, and A. Sotelo, "Decrease of Electrical Resistivity in Ca3co4o9 Thermoelectric Ceramics by Ti Doping," *J. Mater. Sci.: Mater. Electron.,* **26** [2] 815-20 (2015).

23. G. Constantinescu, S. Rasekh, M. Torres, P. Bosque, J. Diez, M. Madre, and A. Sotelo, "Effect of Na Doping on the $Ca_3Co_4O_9$ Thermoelectric Performance," *Ceram. Int.,* **41** [9] 10897-903 (2015).

24. J. Van Landuyt, "Shear Structures and Crystallographic Shear Propagation," *J. Phys. Colloq.,* **35** [C7] C7-53-C7-63 (1974).

25. J. Anderson and B. Hyde, "On the Possible Role of Dislocations in Generating Ordered and Disordered Shear Structures," *J. Phys. Chem. Solids,* **28** [8] 1393-408 (1967).

26. S. Andersson, "The Crystal Structure of $Ti_5O_9$," *Acta Chem. Scand.,* **14** [5] 1161-72 (1960).

27. Y. Le Page and P. Strobel, "Structural Chemistry of the Magnéli Phases $Ti_nO_{2n-1}$, $4 \leq N \leq 9$: Ii. Refinements and Structural Discussion," *J. Solid State Chem.,* **44** [2] 273-81 (1982).

28. L. Bursill and B. Hyde, "Crystal Structures in the {132} CS Family of Higher Titanium Oxides $Ti_nO_{2n-1}$," *Acta Crystallogr. Sect. B: Struct. Crystallogr. Cryst. Chem.,* **27** [1] 210-5 (1971).

29. R. Gibb and J. Anderson, "Electron Microscopy of Solid Solutions and Crystallographic Shear Structures. Ii. $Fe_2O_3$-$TiO_2$ and $Ga_2O_3$-$TiO_2$ Systems," *J. Solid State Chem.,* **5** [2] 212-25 (1972).

30. S. Kamiya and R. Tilley, "Phase Relations in the Pseudobinary System $TiO_2$-$Ga_2O_3$," *J. Solid State Chem.,* **22** [2] 205-16 (1977).

31. D. Lloyd, I. Grey, and L. Bursill, "The Structure of $Ga_4Ti_{21}O_{48}$," *Acta Crystallogr. Sect. B: Struct. Crystallogr. Cryst. Chem.,* **32** [6] 1756-61 (1976).

32. L. Bursill, "Structural Relationships between B-Gallia, Rutile, Hollandite, Psilomelane, Ramsdellite and Gallium Titanate Type Structures," *Acta Crystallogr. Sect. B: Struct. Crystallogr. Cryst. Chem.,* **35** [3] 530-8 (1979).

33. L. Bursill and G. Stone, "Determination of the Displacement Vector at (210) Boundaries in Gallia-Doped Rutile," *Philos. Mag.,* **32** [6] 1151-8 (1975).

34. J. W. Amoroso and D. D. Edwards, "Phase Formation and Stability of Polycrystalline $Na_XGa_{4+X}Ti_{1-X}O_8$,(X~ 0.7)," *Solid State Ionics,* **179** [21] 878-80 (2008).

35. N. Empie and D. Edwards, "Phase Stability and Structure of Alkali Doped-Beta-Gallia Rutile Intergrowths," *Solid State Ionics,* **177** [1] 77-87 (2006).

36. A. L. Jaromin and D. D. Edwards, "Subsolidus Phase Relationships in the $Ga_2O_3$–$Al_2O_3$–$TiO_2$ System," *J. Am. Ceram. Soc.,* **88** [9] 2573-7 (2005).

37. A. Civera, M. Pavese, G. Saracco, and V. Specchia, "Combustion Synthesis of Perovskite-Type Catalysts for Natural Gas Combustion," *Catal. Today,* **83** [1] 199-211 (2003).

38. J. Kingsley, K. Suresh, and K. Patil, "Combustion Synthesis of Fine Particle Rare Earth Orthoaluminates and Yttrium Aluminum Garnet," *J. Solid State Chem.,* **88** [2] 435-42 (1990).

39. C. Bacalski, M. Cherry, G. Hirata, J. McKittrick, and J. Mourant, "The Effects of Fuel-to-Oxidizer Ratio on Luminescence Properties and Particle Morphology of Combustion-Synthesized Europium-Activated Barium Magnesium Aluminate," *JSID,* **1** 93-8 (2000).

40. H. Tuller and A. Nowick, "Small Polaron Electron Transport in Reduced $CeO_2$ Single Crystals," *J. Phys. Chem. Solids,* **38** [8] 859-67 (1977).

41. N. A. Deskins and M. Dupuis, "Electron Transport Via Polaron Hopping in Bulk $TiO_2$: A Density Functional Theory Characterization," *Phys. Rev. B,* **75** [19] 195212 (2007).

42. R. J. D. Tilley, *Defects in Solids*. Wiley, 2008.

43. Q. Zhu, E. M. Hopper, B. J. Ingram, and T. O. Mason, "Combined Jonker and Ioffe Analysis of Oxide Conductors and Semiconductors," *J. Am. Ceram. Soc.,* **94** [1] 187-93 (2011).

44. M. Mapa and C. S. Gopinath, "Combustion Synthesis of Triangular and Multifunctional $ZnO_{1-X}N_X$ ($X \leq 0.15$) Materials," *Chem. Mater.,* **21** [2] 351-9 (2008).

45. S. Söllradl, M. Greiwe, V. J. Bukas, M. R. Buchner, M. Widenmeyer, T. Kandemir, T. Zweifel, A. Senyshyn, S. Günther, and T. Nilges, "Nitrogen-Doping in ZnO Via Combustion Synthesis?," *Chem. Mater.,* **27** [12] 4188-95 (2015).

46. H. Liu, S. S. Thind, G. Wu, J. Wen, and A. Chen, "Synthesis and Photoelectrochemical Studies of N, Zr Co-Doped Mesoporous Titanium Dioxide," *J. Electroanal. Chem.,* **736** 93-100 (2015).

47. A. D. Mani, B. R. Raju, N. Xanthopoulos, P. Ghosal, B. Sreedhar, and C. Subrahmanyam, "Effect of Fuels on Combustion Synthesis of $TiO_2$–Towards Efficient Photocatalysts for Methylene Blue Oxidation and Cr (Vi) Reduction under Natural Sunlight," *Chem. Eng. J.,* **228** 545-53 (2013).

48. S. S. Thind, G. Wu, and A. Chen, "Synthesis of Mesoporous Nitrogen–Tungsten Co-Doped $TiO_2$ Photocatalysts with High Visible Light Activity," *Appl. Catal., B,* **111** 38-45 (2012).

49. S. S. Thind, G. Wu, M. Tian, and A. Chen, "Significant Enhancement in the Photocatalytic Activity of N, W Co-Doped $TiO_2$ Nanomaterials for Promising Environmental Applications," *Nanotechnology,* **23** [47] 475706 (2012).

50. M. Batzill, E. H. Morales, and U. Diebold, "Influence of Nitrogen Doping on the Defect Formation and Surface Properties of $TiO_2$ Rutile and Anatase," *Phys. Rev. Lett.,* **96** [2] 026103 (2006).

51. S. A. Chambers, S. H. Cheung, V. Shutthanandan, S. Thevuthasan, M. K. Bowman, and A. G. Joly, "Properties of Structurally Excellent N-Doped $TiO_2$ Rutile," *Chem. Phys.,* **339** [1] 27-35 (2007).

52. S. H. Cheung, P. Nachimuthu, A. G. Joly, M. H. Engelhard, M. K. Bowman, and S. A. Chambers, "N Incorporation and Electronic Structure in N-Doped $TiO_2$ (110) Rutile," *Surf. Sci.,* **601** [7] 1754-62 (2007).

53. C. Di Valentin, E. Finazzi, G. Pacchioni, A. Selloni, S. Livraghi, M. C. Paganini, and E. Giamello, "N-Doped $TiO_2$: Theory and Experiment," *Chem. Phys.,* **339** [1] 44-56 (2007).

54. I. Tsuyumoto, T. Hosono, and M. Murata, "Thermoelectric Power in Nonstoichiometric Orthorhombic Titanium Oxides," *J. Am. Ceram. Soc.,* **89** [7] 2301-3 (2006).

55. J. Lynch, C. Giannini, J. K. Cooper, A. Loiudice, I. D. Sharp, and R. Buonsanti, "Substitutional or Interstitial Site-Selective Nitrogen Doping in $TiO_2$ Nanostructures," *J. Phys. Chem. C,* **119** [13] 7443-52 (2015).

56. A. Shaula, V. Kharton, N. Vyshatko, E. Tsipis, M. Patrakeev, F. Marques, and J. Frade, "Oxygen Ionic Transport in $SrFe_{1-Y}Al_YO_{3-\Delta}$ and $Sr_{1-X}Ca_XFe_{0.5}Al_{0.5}O_{3-\Delta}$ Ceramics," *J. Eur. Ceram. Soc.,* **25** [4] 489-99 (2005).